第 20 回
核燃焼プラズマ
統合コード研究会

20th Burning Plasma Simulation Initiative (BPSI) Meeting

日時：2023 年 1 月 5 日(木)－6 日(金)
場所：九州大学筑紫キャンパス応用力学研究所
2 階大会議室　および　オンライン

(Ver. 1, 2023 年 2 月 15 日発行)

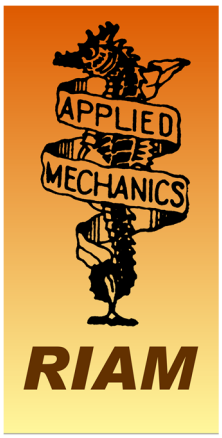

合同会合

第 20 回核燃焼プラズマ統合コード研究会

20th Burning Plasma Simulation Initiative (BPSI) Meeting

および

核融合エネルギーフォーラムサブクラスター会合
シミュレーションクラスター　炉心プラズマモデリングサブクラスター
プラズマ物理クラスター　定常運転・制御サブクラスター

(Ver.3)

日時：2023 年 1 月 5 日(木)－6 日(金)
場所：九州大学筑紫キャンパス　応用力学研究所 2 階大会議室　および　オンライン

1 月 5 日(木)

(核融合エネルギーフォーラムサブクラスターとの合同会合)
9:30 – 9:40　林（QST）
　　連絡事項
9:40 – 10:10　宮戸（QST）
　　IFERC 計算機シミュレーションセンターの現状報告
10:10 – 10:40　横山（核融合研)、林（QST）
　　ITER に於ける統合モデリング活動の報告
10:40 – 11:10　若月（QST）
　　ITPA 統合運転シナリオグループ活動報告
11:10 – 11:30　星野（慶應大）
　　炉心プラズマ＋炉工学炉材料モデリングサブクラスター合同会合の報告
11:30 – 12:00　林（QST）
　　今後の予定の議論

12:00 – 13:30　昼休み

ワークショップ「不純物輸送」 Lunch time workshop “Impurity transport”
13:00 – 13:30 林 (QST)、藤田 (名大)、糟谷 (九大) online
昨年の企画セッションを受けた共同研究作業会を昼休みに開催します
(関係者による集まりですので、自分は関係者だと思われる方ご参加ください)

13:30 – 13:40　事務連絡 Business announcement

（座長：村上)
13:40 – 14:05　講演 1-1　　成田（QST)

Improvement in a semi-empirical turbulent transport model for its versatility and its application to integrated simulations

14:05 – 14:30　講演 1-2　　福山（京大）
Progress of the development of TASK code and interface to IMAS

14:30 – 14:55　講演 1-3　　横山（核融合研）
Introduction to IAEA coordinated research program: AI for Fusion

14:55 – 15:15　講演 1-4　　森下（京大）
Control of LHD plasma using the data assimilation system ASTI

15:15 – 15:25　休憩

(座長：横山)

15:25 – 15:50　講演 1-5　　藤田（名大) online
Study on operation scenario with enhanced radiation power from main plasma by impurity injection in DEMO

15:50 – 16:10　講演 1-6　　持永（九大）
Impurity transport simulation in tokamak plasmas using the integrated code TASK

16:10 – 16:30　講演 1-7　　Park (SNU)
Integrated modelling of high-temperature fusion plasma regime facilitated by fast ions in the KSTAR tokamak

16:30 – 16:45　講演 1-8　　竹本（名大) online
Validation of tungsten transport model by simulating soft x-ray measurement in JT-60U

16:45 – 16:55　休憩

(座長：糟谷)

16:55 – 17:20　講演 1-9　　Hahm (SNU)
ExB vortex dynamics inside a magnetic island

17:20 – 17:45　講演 1-10　　矢木（QST)
Particle transport in fusion plasmas

17:45 – 18:10　講演 1-11　　Choi (SNU) online
Gyrokinetic simulation of KSTAR AE-ETG system

18:10 – 18:35　講演 1-12　　登田（核融合研)
Study of turbulent transport in trapped electron and ion temperature gradient modes in high collision regime for tokamak plasmas

18:50　散会

1 月 6 日(金)

9:00 – 10:30　ポスター講演 Poster
（online, 開室 start 8:45、閉室 end 13:00）

10:30 – 10:40　休憩

（座長：村上）
10:40 – 10:55　講演 1-13　　麝嶋（日大）
Estimation of 2D distribution evolution of electrostatic potential fluctuations using deep learning
10:55 – 11:20　講演 2-1　　滝塚（阪大）online
Several low-cost techniques for global plasma simulation with particle-in-cell model
11:20 – 11:45　講演 2-2　　沼波（核融合研）
Manifold structure appearing in plasma turbulence simulations and transport modeling

(Session Leader：村上)
11:45 – 12:05　議論 Discussion

12:05 – 12:10　事務連絡 Business announcement

12:10 – 13:20　昼休み

(特定研究「計測・シミュレーション・モデリングを組み合わせた統合診断」研究集会との合同会合)
（座長：糟谷）
13:20 - 13:30　講演 3-1　　糟谷（九大）
特定研究「計測・シミュレーション・モデリングを組み合わせた統合診断」の紹介
13:30 - 14:00　講演 3-2　　糟谷（九大）
Global structure and its diagnostic simulation in magnetized plasmas
磁化プラズマにおける巨視的構造診断のためのシミュレーション
14:00 - 14:30　講演 3-3　　本多（京大）
Carbon impurity modeling with the superstage model in TASK/TX
スーパーステージモデルを用いた TASK/TX における炭素不純物モデリング
14:30 – 15:00　講演 3-4　　佐々木（日大）
Study on spatio-temporal dynamics in turbulence applying data-driven science
データ駆動科学による乱流時空間ダイナミクスの研究
15:00 – 15:30　講演 3-5　　山田（九大）
Analysis of turbulent structures in magnetized cylindrical plasmas
直線磁化プラズマにおける乱流構造の解析

15:30 – 16:00　糟谷（九大）
discussion 議論

16:00　散会

Poster number

20th BPSI meeting (2023.1)
(Ver.3)

PA-1 村上定義（京大) S. Murakami
Effects of magnetic and electrostatic fluctuations on ECH supra-thermal electron behavior and toroidal torque in tokamak plasma

PA-2 轟晴彦（九大) H. Todoroki
Analysis of turbulent particle fluxes by using 5-field RMHD code in torus plasmas

PA-3 梅崎大介（九大工) D. Umezaki
Effect of large-angle scattering transport in divertor plasmas

PA-4 矢本昌平（量研) S. Yamoto
Improvements of impurity transport modelling by integrated divertor code SONIC and its application to predictive simulation of future devices

PA-5 吉原稜（九大) R. Yoshihara
Simulation of 3D perturbation measurement in torus plasmas using a heavy ion beam probe

PA-6 古田原拓実（日大) T. Kodahara
Analysis of particle transport in PANTA by using multi-field SVD

PA-7 田原康祐（京大) K. Tahara
Influence of the beam-beam collisions on the energetic particle distribution in Large Helical Device

Improvement in a semi-empirical turbulent transport model for its versatility and its application to integrated simulations

E. Narita[1], M. Honda[2], M. Nakata[3,4], M. Yoshida[1], N. Hayashi[1] and T. Nakayama[4]

[1]National Institutes for Quantum Science and Technology, Naka, Ibaraki 311-0193, Japan

[2]Graduate School of Engineering, Kyoto University, Nishikyo, Kyoto 615-8530, Japan

[3]National Institute for Fusion Science, Toki, Gifu 509-5292, Japan

[4]The Graduate University for Advanced Studies, Toki, Gifu 509-5292, Japan

1 Introduction

Neural network (NN) based turbulent transport models have been introduced to predict temperature and density profiles quickly. Such models successfully predict turbulent fluxes 10^{3-5} times faster than the conventional reduced models, such as TGLF [1,2], and they are now utilized practically. While most NN based turbulent transport models are surrogate models, which are built to mimic the reduced models, our model named DeKANIS [3-5] is based on gyrokinetic calculation results and experimental data.

DeKANIS predicts turbulent particle and heat fluxes for electrons in a quasilinear limit as $\bar{\Gamma}_\mathrm{e} = \bar{D}\left(\frac{R}{L_{n_\mathrm{e}}} + C_\mathrm{T}\frac{R}{L_{T_\mathrm{e}}} + C_\mathrm{P}\right)$ and $\bar{Q}_\mathrm{e} = \bar{\chi}_\mathrm{e}\left(C_\mathrm{N}\frac{R}{L_{n_\mathrm{e}}} + \frac{R}{L_{T_\mathrm{e}}} + C_\mathrm{HP}\right)$, respectively. Here, non-dimensional $\bar{D}$, $\bar{\chi}$, R/L_n and R/L_T are the particle and heat diffusivities in proportion to fluctuation amplitudes and the density and temperature gradients, respectively. The fluxes are composed of the diagonal (diffusive) and off-diagonal (non-diffusive) terms, which are quantitatively determined by calculating the off-diagonal-term coefficients ($C_\mathrm{T,P,N,HP}$) and the diffusivities ($\bar{D}$ and $\bar{\chi}_\mathrm{e}$). In addition to the electron fluxes, DeKANIS predicts the ion heat flux, which is given as $\bar{Q}_\mathrm{i} = \frac{\bar{\chi}_\mathrm{i,eff}}{\bar{\chi}_\mathrm{e,eff}}\bar{\chi}_\mathrm{e,eff}\frac{R}{L_{T_\mathrm{i}}}\frac{n_\mathrm{i}}{n_\mathrm{e}}\frac{T_\mathrm{i}}{T_\mathrm{e}}$. Here, $\bar{\chi}_\mathrm{eff}$ is the normalized effective heat diffusivity. Once $\bar{\chi}_\mathrm{e,eff}$ is obtained with $\bar{Q}_\mathrm{e}$, $\bar{Q}_\mathrm{i}$ can be constructed through $\bar{\chi}_\mathrm{i,eff}/\bar{\chi}_\mathrm{e,eff}$. To forecast $\bar{\Gamma}_\mathrm{e}$, $\bar{Q}_\mathrm{e}$ and $\bar{Q}_\mathrm{i}$, the NN model and the scaling formula are utilized. The NN model was trained to evaluate $C_\mathrm{T,P,N,HP}$ and $\bar{\chi}_\mathrm{i,eff}/\bar{\chi}_\mathrm{e,eff}$, whose training datasets are prepared by the linear gyrokinetic calculations with GKW [6] at the normalized wavenumber $\bar{k}_\theta$ with the normalized maximum linear growth rate $\bar{\gamma}_\mathrm{max}$ of the ion temperature gradient (ITG) mode or the ITG/trapped electron mode (TEM). The NN model also predicts the corresponding $\bar{k}_\theta$ and $\bar{\gamma}_\mathrm{max}$, which are passed to the scaling formula to determine $\bar{D}$. The remaining coefficient, $\bar{\chi}_\mathrm{e}$, is calculated with the relationship between $\bar{D}$ and $\bar{\chi}_\mathrm{e}$: $\bar{\chi}_\mathrm{e} = \bar{D}(C_\mathrm{T} + 1.5)/C_\mathrm{N}$.

In this paper, the NN training datasets and the scaling formula are modified for the versatility of DeKANIS, and it is applied to integrated simulations of an ITER pre-fusion power operation 1 (PFPO-1) plasma [5].

2 Expansion of training data

The training datasets of the previous NN model were based on JT-60U H-mode plasmas, whose ion temperatures are higher than the electron ones: $T_\mathrm{e}/T_\mathrm{i} < 1$, at most radial points. Also, the

datasets cover the plasma parameters in $0.30 \leq \rho \leq 0.65$. To apply DeKANIS to predictions of the high-performance plasmas, it needs to be applicable to the range including $T_\mathrm{e}/T_\mathrm{i} \gtrsim 1$ since alpha particles primarily heat electrons in burning plasmas, electron cyclotron (EC) heating is envisaged in the PFPO-1 phase, and the collisional equipartition leads to $T_\mathrm{e}/T_\mathrm{i} \sim 1$ in high density plasmas. When it comes to estimating the performance including the edge pedestal region, DeKANIS needs to give the turbulent fluxes also in the outer core region, $0.65 \leq \rho \leq 0.85$. To this end, a subset of JET plasmas [7] has been introduced, whose $T_\mathrm{e}/T_\mathrm{i}$ is around or exceeds unity, and the outermost radial point has changed from $\rho = 0.65$ to $\rho = 0.85$.

3 Modification of the saturation model

The previous DeKANIS determined $\bar{D}$ with the following scaling formula: $\bar{D}_\mathrm{model,pre} \propto \left(\bar{\gamma}/\bar{k}_\theta^2\right)^\alpha \left[K_\mathrm{RH}\left(\bar{\gamma}/\bar{k}_\theta^2\right)^{0.5}\right]^{-\beta}$. Here, the normalized quasilinear diffusivity $\bar{\gamma}/\bar{k}_\theta^2$ characterizes turbulent transport, and the suppression of instabilities due to zonal flows is expressed with the linear zonal flow response function K_RH given as $K_\mathrm{RH} = 1/(1 + 1.6q^2/\epsilon^{0.5})$ [8] and the proxy of the zonal flow potential, $\left(\bar{\gamma}/\bar{k}_\theta^2\right)^{0.5}$, where q and ϵ are the safety factor and the inverse aspect ratio, respectively. The exponents α and β were optimized by the regression analysis to reproduce $\bar{D}_\mathrm{exp}$, which is semi-empirically estimated with the electron heat flux of the JT-60U plasmas, and $\alpha = 1.32$ and $\beta = 2.93$ were obtained. As displayed in figure 1(a), the previous model shows a high mean squared logarithmic error (MSLE) of 0.322 for JT-60U regression data, and underestimates test data given by the JET plasmas. Furthermore, the net exponent of $\bar{\gamma}/\bar{k}_\theta^2$ is negative, $\alpha - 0.5\beta = -0.145$, which contradicts the mixing-length theory.

Since one of the questions of the previous model is that K_RH was derived in the collisionless limit, collisional decay of the zonal flows is introduced with $\bar{\tau}_\mathrm{r}$. Here, $\bar{\tau}_\mathrm{r} = \left(\nu_\mathrm{f}^2/\omega_\mathrm{f}^2 + K_\mathrm{RH}^2\omega_\mathrm{f}^2/\nu_\mathrm{d}^2\right)^{0.5}$, and the square of it measures the suppression of turbulence by zonal flows considering its collisional damping [9], where $\omega_\mathrm{f} = v_\mathrm{th,i}/R$, $\nu_\mathrm{f} = \omega_\mathrm{f}\exp\left(-q^2\right)$, $\nu_\mathrm{d} = 0.67/\left(\tau_\mathrm{ii}\epsilon\right)$ with the ion thermal velocity $v_\mathrm{th,i}$, the major radius R and the ion-ion collision time τ_ii. The new scaling formula uses $\bar{\tau}_\mathrm{r}$ instead of K_RH: $\bar{D}_\mathrm{model,new} \propto \left(\bar{\gamma}/\bar{k}_\theta^2\right)^\alpha \left[\bar{\tau}_\mathrm{r}\left(\bar{\gamma}/\bar{k}_\theta^2\right)^{0.5}\right]^{-\beta}$. The optimized exponents are $\alpha = 0.755$ and $\beta = 1.20$, and the net exponent of $\bar{\gamma}/\bar{k}_\theta^2$ is positive, $\alpha - 0.5\beta = 0.155$. The value is small, but the new model is better than the previous one in terms of the mixing-length theory. As shown in figure 1(b), the MSLE decreases for regression data, and the tendency to underestimate $\bar{D}_\mathrm{exp}$ of test data is no longer observed. The increase in the MSLE for test data is due to the data points with a high collision frequency, namely, $\nu_\mathrm{ii}^* > 0.1$. Since enough regression data were not collected in $\nu_\mathrm{ii}^* > 0.1$, the model predicts too large $\bar{D}$ because of the too suppressed $\bar{\tau}_\mathrm{r}$ for the data points in question. The MSLE is reduced without such data points.

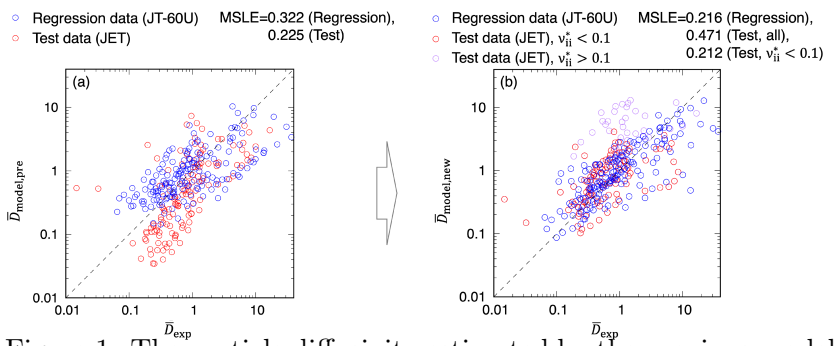

Figure 1. The particle diffusivity estimated by the previous model (a) $\bar{D}_\mathrm{model,pre}$ and the new model (b) $\bar{D}_\mathrm{model,new}$ compared with $\bar{D}_\mathrm{exp}$ for regression and test data.

4 An integrated simulation of an ITER PFPO-1 plasma

The modified DeKANIS is implemented in the integrated model GOTRESS+ [10] to perform a core-pedestal coupling integrated simulation of an ITER PFPO-1 plasma with the plasma current of 5.0MA and the toroidal magnetic field of 1.8T. To solve heat transport in the core region, $\rho \leq 0.85$, DeKANIS gives the turbulent fluxes and Matrix Inversion method gives the neoclassical ones. The pedestal height is determined with the in-house EPED1 model, and the equilibrium and current profile alignment code ACCOME is also contained. The density profile is prescribed. When the plasma is heated by EC heating with 20MW, the electron and ion temperatures are obtained as shown in figure 2(a) after eight iterations. As the turbulent fluxes near the magnetic axis are computed by extrapolation, the temperatures in $\rho \geq 0.25$ are compared with those predicted by the previous study using TGLF [11], which shows $T_\mathrm{e} \sim 10$keV and T_i 5.5keV at $\rho = 0.3$ and $T_\mathrm{e,i} \sim 3.5$keV at $\rho = 0.8$. Our simulation predicts similar temperature profiles. In forecasting the turbulent fluxes, DeKANIS calculates the off-diagonal term coefficients, which can be verified with GKW as shown in figure 2(b). The first off-diagonal term, $C_\mathrm{N} R/L_{n_\mathrm{e}}$, given by DeKANIS is close to that of GKW, while the second one, C_HP, is overestimated. Since C_HP estimated by DeKANIS and GKW are both smaller than the other two terms, it can be said that turbulent transport is mostly caused by the diagonal term and the off-diagonal one driven by the density gradient and that the two terms produce turbulent fluxes with the similar level.

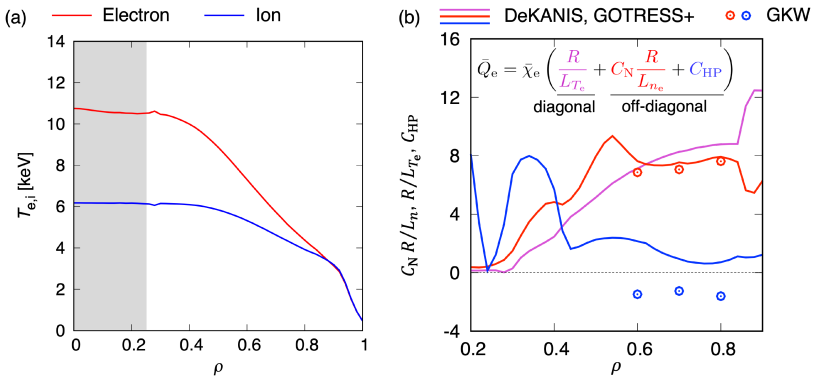

Figure 2. (a) The temperature and (b) the diagonal and off-diagonal term profiles predicted by the integrated simulation with DeKANIS implemented in GOTRESS+ for the ITER PFPO-1 plasma. In the subfigure (b), the results are verified with GKW.

References

[1] G.M. Staebler *et al.,* Phys. Plasmas **12** 102508 (2005).
[2] G.M. Staebler *et al.,* Nucl. Fusion **61** 116007 (2021).
[3] E. Narita *et al.,* Nucl. Fusion **59** 106018 (2019).
[4] E. Narita *et al.,* Nucl. Fusion **61** 116041 (2021).
[5] E. Narita *et al.,* Contrib. Plasma Phys. e202200152 (2023).
[6] A.G. Peeters *et al.,* Comput. Phys. Commun. **180** 2650 (2009).
[7] The ITER 1D Modelling Working Group, Nucl. Fusion **40** 1955 (2000).
[8] M.N. Rosenbluth and F.L. Hinton, Phys. Rev. Lett. **80** 724 (1998).
[9] F.L. Hinton and M.H. Rosenbluth, Plasma Phys. Control. Fusion **41** A653 (1999).
[10] M. Honda *et al.,* Nucl. Fusion **61** 116029 (2021).
[11] A. Loarte *et al.,* Nucl. Fusion **61** 076012 (2021).

Introduction to IAEA coordinated research program (CRP): AI for Fusion (AI4F)

M. Yokoyama
National Institute for Fusion Science, Rokkasho Research Center

The IAEA organized the Technical Meeting on Artificial Intelligence (AI) for Nuclear Technology and Applications (#AI4Atoms) on 25–29 October 2021, to programmatically discuss to form the roadmap for IAEA role & support in use of AI in nuclear science, technology, and applications. It consisted of 10 working groups (WGs) along with cross-cutting groups (enabling infrastructure, and advanced modelling and simulation methodologies). There is a "Nuclear Fusion" WG (NFWG) in 10 WGs.

Prof. Hideo Nagatomo (Osaka University) and I (Masayuki Yokoyama) joined this NFWG from Japan, to launch continuously discuss to form the Coordinated Research Project (CRP). It resulted in the launch of CRP on AI for Accelerating Fusion R&D (2022–2027) with the objective of accelerating fusion R&D with Machine Learning (ML)/AI, through the creation of a platform and cross-community network for innovation and partnership. (cf., https://nucleus.iaea.org/sites/ai4atoms/ai4fusion/SitePages/What-is-AI-for-Fusion-.aspx?web=1)

This CRP is composed by four Work Packages (WP), as follows.

WP 1: Real-time MFE System Behaviour Prediction, Identification & Optimization Using ML/AI Methods (MFE: Magnetic Fusion Energy)

WP 2: IFE Physics Understanding through Simulation, Theory and Experiment Using ML/AI Methods (IFE: Inertial Fusion Energy)

WP 3: Feasibility of MFE and IFE Image Database

WP 4: Community Engagement & Workforce Development

The objectives, expected activities/output/outcomes for each WP are described on the above-mentioned webpage.

This information was distributed via the mailing list of The Japan Society of Plasma Science and Nuclear Fusion Research, for calling the proposal from institutions/universities in Japan. Then, Osaka University and NIFS individually applied, and they were approved by the IAEA.

Below, only contents of the **application from NIFS** are introduced (referring the application).

Title of the research agreement

Radiation-collapse discharge database from Large Helical Device (LHD)

Summary of the proposed research

Radiation-collapse discharge database will be provided from Large Helical Device (LHD), as a part of this internationally coordinated research program. This should accelerate fusion R&D via ML/AI applications regardless the differences on confinement concepts in MFE. In particular, provided database should be a common ground for developing anomaly detection methods via ML/AI.

Description of research objectives and anticipated outcomes

To accelerate fusion R&D by establishing a multi-machine database of experimental MFE data (adhering to FAIR/Open Science principles) for ML/AI-driven applications, and through increased access to knowledge and information of ML/AI methods for MFE. Radiation-collapse discharge database could be provided from Large Helical Device (LHD). This should accelerate fusion R&D via ML/AI applications regardless the differences on confinement concepts in MFE.

Scientific scope of the project

Concrete contribution to WP1 by providing radiation-collapse discharge database of LHD, as a part of multi-machine database of experimental MFE data for ML/AI applications.

Expected Outputs

* Accelerate fusion R&D via ML/AI application.
* Ensured data reproducibility and accessibility for across domains for the international community.
* Increase access to knowledge and information about ML/AI for MFE R&D.

The progress and on-going activities within this CRP framework will be reported as they become available.

Impurity transport simulation in tokamak plasmas using the integrated code TASK

S. Mochinaga[1)], N. Kasuya[1,2)], A. Fukuyama[3)] and M. Yagi[4)]

[1)] IGES, Kyushu University, [2)] RIAM, Kyushu University, [3)]Kyoto University, [4)]QST

1. Introduction

Negative magnetic shear mode and high β_p mode are improved confinement modes, which can achieve high plasma performance with the formation of an internal transport barrier (ITB) in the core plasma. However, the ITB region can increase accumulation of impurities in the core plasma, which may lead to plasma collapse [1,2]. Tungsten produced from metal walls and divertor plates induce particularly large radiation losses, so the accumulation in the core plasma should be avoided. One of the factors that accelerates the tungsten accumulation is inward neoclassical pinch component driven by bulk ion density gradient [3]. Some studies have shown that electron cyclotron heating suppresses inward impurity transport by increasing the bulk temperature gradient and decreasing the density gradient [4]. In this study, simulations are performed by focusing on neoclassical transport, which may accelerate impurity accumulation in the ITB region, and the mechanism of tungsten profile formation is investigated.

.

2. Transport simulation models

The TASK code is one of the integrated codes developed in Japan, which has a modular structure combining many codes such as equilibrium, transport, and wave analysis. The multiple modules exchange data through the data interface BPSD [5], which enables self-consistent simulations of time evolutions of plasma variables.

In the transport calculations of plasma main component using the TASK/TR code, the following diffusive one-dimensional equations for particle and heat transport are solved [6].

$$\frac{1}{V'}\frac{\partial}{\partial t}(n_s V') = -\frac{1}{V'}\frac{\partial (V'\Gamma_S)}{\partial \rho} + S_s\,, \tag{1}$$

$$\frac{1}{V'^{5/3}}\frac{\partial}{\partial t}\left(\frac{3}{2}n_s T_s V'^{5/3}\right) = -\frac{1}{V'}\frac{\partial (V' Q_S)}{\partial \rho} + P_s\,, \tag{2}$$

Here, n_s is the plasma density, T_s is the plasma temperature, S_s is the particle source, P_s is the heat source, ρ is the normalized radius, V' is the radial derivative of plasma volume, and s is the index representing plasma species as ion and electron. The particle flux Γ_s and heat flux Q_s are given as follows;

$$\Gamma_s = \langle|\nabla\rho|\rangle V_s n_s - \langle|\nabla\rho|^2\rangle D_s \frac{\partial n_s}{\partial \rho}, \tag{3}$$

and

$$Q_s = \langle|\nabla\rho|\rangle \frac{3}{2} n_s T_s V_{E_s} - \langle|\nabla\rho|^2\rangle n_s \chi_s \frac{\partial T_s}{\partial \rho} + \frac{3}{2}\Gamma_S T_s\,. \tag{4}$$

Here, $<|\nabla\rho|>$, $<|\nabla\rho|^2>$ are the metric values, V_s is the particle convective velocity, D_s is the particle diffusion coefficient, V_{Es} is the heat convective velocity, and χ_s is the heat diffusion coefficient. The diffusion coefficients are given by linear summation of neoclassical and turbulent diffusion coefficients, and the convective velocities consist of the neoclassical component only. For the neoclassical transport model, NCLASS [7] is applied. For the turbulent transport model, CDBM (Current Diffusive Ballooning Mode) or mBgB (mixed Bohm and gyro Bohm) models are applied. The diffusion coefficients by the CDBM model are as the followings [8,9];

$$\chi_{CDBM} = \chi_e = \chi_i = F(s,\alpha)\alpha^{1.5}\frac{c^2}{\omega_{pe}^2}\frac{v_A}{qR}, \tag{5}$$

$$D_e = D_i = \frac{1}{2}\chi_{CDBM}, \tag{6}$$

where, c is the speed of light, ω_{pe} is the electron plasma frequency, v_A is the Alfvén velocity, q is the safety factor, $s \equiv (r/q)(dq/dr)$ is the magnetic shear, $\alpha \equiv -(2\mu_0 q^2 R/B^2)(dp/dr)$ is the normalized pressure gradient. The shaping factor $F(s,\alpha)$ is defined as

$$F(s,\alpha) = \frac{1}{\sqrt{2(1-2s')\left(1-2s'+3s'^2\right)}}\,(s' = s - \alpha < 0), \tag{7}$$

$$F(s,\alpha) = \frac{1 + 9\sqrt{2}s'^{5/2}}{\sqrt{2}\left(1 - 2s' + 3s'^{2} + 2s'^{3}\right)} (s' = s - \alpha \geq 0).$$

$F(s,\alpha)$ decreases rapidly when s-α becomes smaller than 0.75. The stabilizing effect of $E \times B$ flow shear is not considered in this study. On the other hand, the mBgB model can be expressed as follows [10,11].

$$\chi_e = 8.0 \times 10^{-5}\chi_B + 3.5 \times 10^{-2}\chi_{gB}, \quad (8)$$

$$\chi_i = 1.6 \times 10^{-4}\chi_B + 1.75 \times 10^{-2}\chi_{gB}, \quad (9)$$

$$D_{e,i} = (0.3 + 0.7\rho)\frac{\chi_e\chi_i}{\chi_e + \chi_i}. \quad (10)$$

The Bohm term χ_B and gyro-Bohm term χ_{gB} are given by

$$\chi_B = \rho_s c_s q^2 \frac{a(dp_e/dr)}{p_e}\frac{T_e(\rho = 0.8) - T_e(\rho = 1.0)}{T_e(\rho = 1.0)}\Theta\left(-0.14 + s - \left|\frac{1.47\omega_{E\times B}}{\gamma_{ITG}}\right|\right), \quad (11)$$

$$\chi_{gB} = \rho_s^2 c_s \frac{(dT_e/dr)}{T_e}, \quad (12)$$

where, ρ_s is the gyro radius, c_s is the sound speed, p_e is the electron pressure, Θ is the Heaviside function, $\omega_{E\times B}$ is the E×B flow shear rate and γ_{ITG} is the ITG growth rate. In the impurity transport calculations using the TASK/TI code, the following particle transport equations including atomic processes are solved for k-valent ionized impurity ions.

$$\frac{1}{V'}\frac{\partial}{\partial t}(V'n_k) = -\frac{1}{V'}\frac{\partial}{\partial \rho}(\Gamma_k) + \gamma_{k-1}n_e n_{k-1} - \gamma_k n_e n_k - \alpha_k n_e n_k + \alpha_{k+1}n_e n_{k+1}, \quad (13)$$

$$\frac{1}{V'}\frac{\partial}{\partial t}(V'n_1) = -\frac{1}{V'}\frac{\partial}{\partial \rho}(\Gamma_1) - \gamma_1 n_e n_1 + \alpha_2 n_e n_2 - \alpha_1 n_e n_1 + S_0 \ (k = 1), \quad (14)$$

where, γ_k is the ionization rate, α_k is the recombination rate and S_0 is the impurity source. The particle flux Γ is the same as in Eq. (3), and the turbulent diffusion coefficient is $D_Z = D_i$. The impurity temperatures are assumed to be equivalent to the bulk temperature. The γ_k, α_k and radiation loss power of impurity are evaluated by using OPEN-ADAS [12] database. In this simulation, the impurity source is set for the singly charged impurity ion, assuming that the ion density is n_1 to have thermal velocity v_{th} at the plasma edge. The time evolution of bulk plasmas and impurities is solved by linking the TR and TI modules. The data of plasma density and temperature profiles are transferred from TR to TI, while the data of radiation loss power and effective charge number are transferred from TI to TR.

3. Tungsten transport in negative magnetic shear mode

In this section, the results of negative magnetic shear mode calculations are presented with the parameters referring to JET tokamak; the major radius R = 3.0 m, minor radius a = 1.2 m, ellipticity κ = 1.5, magnetic field B_t = 3.0 T, and on-axis heating power for electrons and ions 5MW. The CDBM model is used for turbulent transport in this calculation. Figure 1 shows the time evolution of the plasma current and heating power. The plasma current is steady to be 3 MA in the corresponding L-mode, but in the negative shear mode calculation, it is ramped up from 1 MA to 3 MA in 1 second. The additional heating of 5 MW is applied at the same time as the current ramp-up. As shown in Fig. 2, the current ramp-up operation causes the OH current to rise from the plasma periphery, resulting in a concave current density profile. Corresponding to the current profile, a negative shear region is formed.

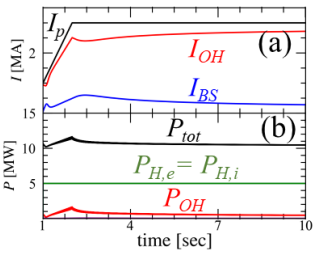

Fig. 1: Time evolution of (a) plasma current and (b) heating power.

The radial profiles of the bulk plasma and impurity are shown in Fig. 3. In the negative shear mode, a strong gradient region is formed in the ion temperature and density profiles. This is because the transport is improved by locally reduced diffusion coefficient in the negative shear region. The formation of the negative magnetic shear is transient, and the ITB moves toward the plasma center with current diffusion, eventually approaching the L-mode state. The temperature increases, because the heating power is greater at the plasma center, and the density decreases, because the particle source is only set at the plasma periphery. When the strong ITB is formed, an inward pinch is driven in the ITB region to increase the tungsten density, resulting to give a step-like profile. This induces a greater amount of impurity accumulation in the plasma core than in the L-mode case. Especially from t = 2 to 3 sec, the tungsten density increases due to large bulk density gradient. For t = 4 sec the bulk density decreases, while the strength of the temperature gradient is maintained, so the tungsten convection directs outward to reduce the tungsten density.

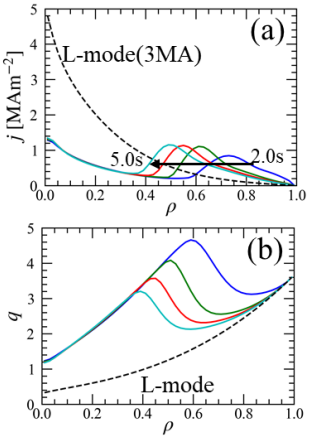

Fig. 2: Radial profiles of (a) current density and (b) safety factor.

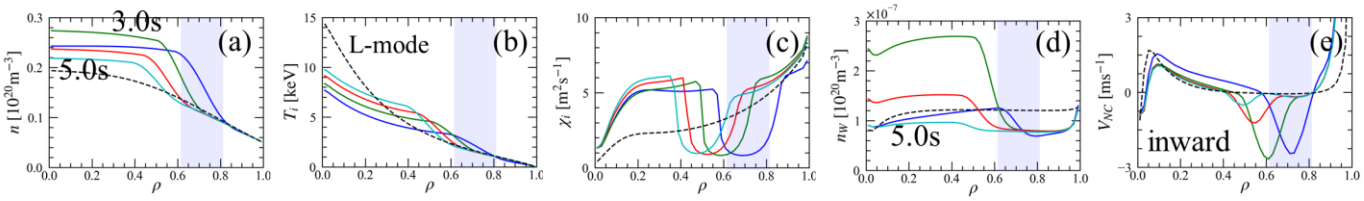

Fig. 3: Radial profiles of (a) plasma density, (b) ion temperature, (c) ion thermal diffusivity, (d)tungsten density and (e) neoclassical pinch.

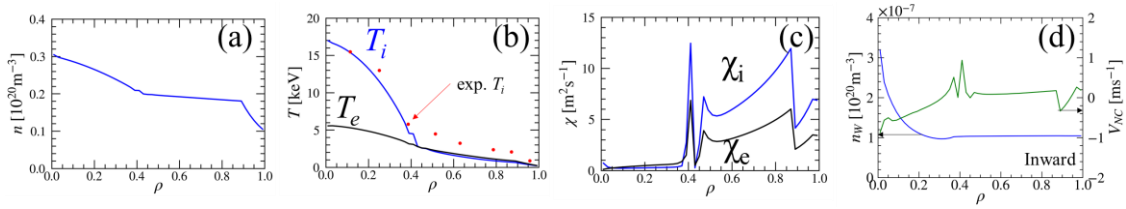

Fig. 4: Radial profiles of (a) plasma density, (b) electron and ion temperature, (c) electron and ion thermal diffusivity, (d) tungsten density and neoclassical pinch.

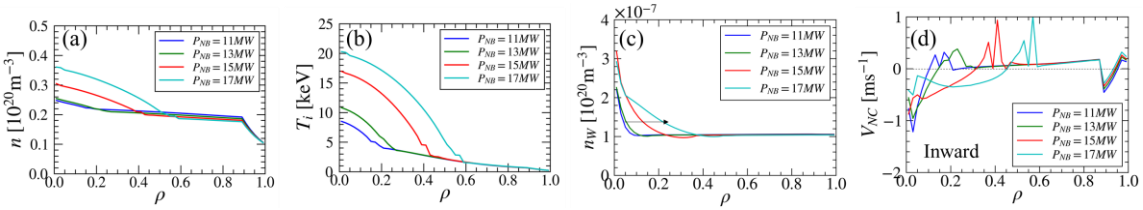

Fig. 5: Radial profiles of (a) plasma density, (b) ion temperature, (c) tungsten density and (d) neoclassical pinch.

4. Tungsten transport in high β_p mode

In this section, the transport calculations for tungsten are carried out with reference to the high β_p mode discharge in JET [13]. The plasma parameters are R = 3.0 m, a = 0.9 m, κ = 1.5, B_t = 2.6 T and I_p = 2.2 MA. Neutral beam injection heating P_{NB} = 15 MW and ion cyclotron heating P_{ICRF} = 5 MW are applied as external current-driven heating sources. As a turbulent model, the mBgB model is used, because it is an empirical model based on JET experiments. Figure 4 shows the radial profiles of bulk plasma and tungsten impurity. The diffusion coefficient decreases due to the influence of the magnetic shear and the E×B flow shear at ρ = 0.0 - 0.4, while there is a peak due to a numerical problem. Inside $\rho < 0.3$, the effect of magnetic shear is strong, and with ρ = 0.3 - 0.4, the stabilizing effect of E×B flow shear makes the ITB-foot position more outward. Only the ion temperature profile is compared with the experimental data, which shows good agreement inside the ITB-foot. However, in the plasma periphery, the values seem to deviate due to the difference in the heating or plasma density profiles. On the other hand, the density profile of tungsten increases near the center of the plasma like the bulk density profile. This is because the diffusion coefficient near the plasma center is smaller and the inward neoclassical pinch component is driven by the NBI particle supply to increase the density gradient.

Calculations are performed for different NBI input power. As shown in Fig. 5, with increasing NBI power, the plasma density and temperature increase due to increased particle supply and heating, which make the transport improvement region wider. For impurities, the inward neoclassical pinch becomes stronger and wider with higher NBI power, and the tungsten density increases over a larger area, resulting in more tungsten accumulation.

5. Conclusion

Tungsten transport calculations in the negative shear mode and high β_p mode are performed using the integrated code TASK. In the negative shear mode, the inward neoclassical pinch component is driven when the plasma density gradient is maintained in the ITB region. Even in the high β_p mode, it results in an increase in tungsten density in the plasma center region where the plasma density gradient is strong. Impurities may accumulate in the plasma core due to the formation of ITB. In the future, impurity control by electron cyclotron heating, which has been confirmed to

be effective in experiments, will be investigated.

This work was supported by JST SPRING, Grant Number JPMJSP2136, and by the collaboration program of QST on development research of the fusion DEMO reactor.

References

[1] R. Dux, *et al*., J. Nucl. Mater. **313,** 1150 (2003).
[2] W. Chen, *et al*., Phy. Lett. A **440,** 128141 (2022).
[3] C. Angioni, *et al*., Nucl. Fus. **54**, 083028 (2014).
[4] R. Neu *et al*., Plasma Phys. Control. Fusion **44**, 811 (2002).
[5] https://bpsi.nucleng.kyoto-u.ac.jp/task/
[6] M. Honda, *et al*., Nucl. Fusion **46**, 580 (2006).
[7] W. Houlberg, *et al*., Phys. Plasmas **4**, 3230 (1997).
[8] M. Yagi, *et al*., Phys. Fluids B **5**, 3702 (1993).
[9] A. Fukuyama *et al*., Plasma Phys. Control. Fusion **37**, 543 (1995).
[10] T. J. J. Tala, *et al*., Plasma Phys. Control. Fusion **43,** 507 (2001).
[11] L. Garzotti, *et al*., Nucl. Fus. **43,** 1829 (2003).
[12] ADAS website, http://www.adas.ac.uk/
[13] P. Buratti, *et al*., Nucl. Fus. **41,** 1809 (2001).

Particle Transport in Fusion Plasmas

M. Yagi

National Institutes for Quantum and Radiological Science and Technology,
Rokkasho Fusion Institute, Rokkasho, Aomori, Japan

1. Introduction

In fusion plasmas, the burn control is important issue to sustain the self-ignition condition. We need to provide fuels externally across the last closed flux surface, at the same time, extract Helium ash from the plasma core. Therefore, to understand particle transport mechanism is a key to develop the burn control method. For fuel injections such as gas puffing or pellet injection, we expect the hollow density profile will be formed in plasma peripheral region. The stabilization of trapped-particle modes by the inverted density gradient was reported [1]. According to local gyrokinetic simulations, we found the inward particle flux was driven by the inverted density gradient in the semi-collisional plasmas [2]. The particle transport driven by the ion-mixing mode [3] was also investigated. We analytically found that the growth rate of electron drift wave driven by the parallel thermal conductivity (semi-collisional effect) and negative η_e is larger than the ion mixing mode with $\eta_i < 0$ limit where $\eta_{i,e}$ implies the ratio of the density gradient scale length to the ion or electron temperature gradient scale length, respectively. However, the question is naturally arisen whether such follow profile is sustained or not under plasma turbulent state, in other words, how long does the source of inward particle flux survive? To answer this question, the global simulation is inevitable. In the present study, the global fluid simulation based on the 6-field drift reduced MHD model is performed which is the extension of 4-field model [4].

2. 6-field drift reduced MHD model

The 6-field drift reduced MHD model is composed of the vorticity equation, the generalized Ohm's law, continuity equation, the parallel momentum equation, the electron temperature evolution equation and ion temperature evolution equation. They are given by

$$\frac{\partial}{\partial t}\nabla_\perp^2 F + [F, \nabla_\perp^2 F] - \delta \nabla_\perp * [p_i, \nabla_\perp F] = -\nabla_\parallel J + \mu_{\perp i}\nabla_\perp^4 F \tag{1}$$

$$\frac{\partial}{\partial t}\left(A - \delta^2 \frac{m_e}{m_i} J\right) = -\nabla_\parallel(\phi - \delta p_e) + \delta^2 \frac{m_e}{m_i}[\phi, J] + \eta_\parallel J - 4\mu_{\perp e}\delta^2 \frac{m_e}{m_i}\nabla_\perp^2 J \tag{2}$$

$$\frac{dn}{dt} + \beta \frac{dp}{dt} = \beta[\Omega, \phi - \delta p_e] - \beta\nabla_\parallel(v + \delta J) + \eta_\perp \beta \nabla_\perp^2 p \tag{3}$$

$$\frac{dv}{dt} = -\nabla_{\parallel}^{(0)} p + [A, p] + 4\mu_{\perp i}\nabla_{\perp}^2 v \tag{4}$$

$$\frac{dT_e}{dt} - \frac{\beta_e}{\beta}\frac{dn}{dt} = -\alpha_T \delta \beta_e \nabla_{\parallel} J + \epsilon^2 \chi_{\parallel e}\nabla_{\parallel}^2 T_e + \chi_{\perp e}\nabla_{\perp}^2 T_e - \frac{5}{2}\delta\beta_e[\Omega, T_e] \tag{5}$$

$$\frac{dT_i}{dt} - \frac{\beta_i}{\beta}\frac{dn}{dt} = \epsilon^2 \chi_{\parallel i}\nabla_{\parallel}^2 T_i + \chi_{\perp i}\nabla_{\perp}^2 T_i + \frac{5}{2}\delta\beta_i[\Omega, T_i] \tag{6}$$

where $F = \phi + \delta p_i,\ J = \nabla_{\perp}^2 A,\ \Omega = 2rcos\theta,\ \delta = \frac{c}{\omega_i a},\ \beta_e = \frac{4\pi p_e}{B^2},\ \beta_i = \frac{4\pi p_i}{B^2},\ \beta = \beta_e + \beta_i,$

$\frac{d}{dt} = \frac{\partial}{\partial t} + [\phi,]$ represents the convective derivative and $\nabla_{\parallel} = \nabla_{\parallel}^{(0)} - [A,]$.

The normalization is performed based on the minor radius a and the poloidal Alfven time $\frac{a}{\epsilon v_A}$ where $\epsilon = a/R_0$ is the inverse aspect ratio, R_0 is the major radius. The energy conservation law is written as

$$\frac{d}{dt}\langle h\rangle = -\langle s\rangle \tag{7}$$

with

$$h = \frac{1}{2}|\nabla_{\perp}F|^2 + \frac{1}{2}|\nabla_{\perp}A|^2 + \frac{1}{2}\delta^2\frac{m_e}{m_i}J^2 + \frac{1}{2}v^2 + \frac{1}{2}p^2 + \frac{1}{2}\frac{n^2}{\beta} + \frac{1}{2}\frac{3T_e^2}{2\beta_e} + \frac{1}{2}\frac{3T_i^2}{2\beta_i} \tag{8}$$

and

$$s = \mu_{\perp i}|\nabla_{\perp}^2 F|^2 + \eta_{\parallel}J^2 + 4\mu_{\perp e}\delta^2\frac{m_e}{m_i}|\nabla_{\perp}J|^2 + \eta_{\perp}\beta|\nabla_{\perp}p|^2 + 4\mu_{\perp i}|\nabla_{\perp}v|^2 + \frac{\epsilon^2\chi_{\parallel e}}{\beta_e}\left|\nabla_{\parallel}T_e\right|^2 +$$

$$\frac{\chi_{\perp e}}{\beta_e}|\nabla_{\perp}T_e|^2 + \frac{\epsilon^2\chi_{\parallel i}}{\beta_i}\left|\nabla_{\parallel}T_i\right|^2 + \frac{\chi_{\perp i}}{\beta_i}|\nabla_{\perp}T_i|^2 \tag{9}$$

where $\langle\cdots\rangle$ represents the volume integral. It should be noted that s is given by the positive definite form [5].

The density source and the sink term were introduced into the continuity equation (3) and the electron temperature evolution equation (5), respectively. Here, we assume that the density source has a sphere shape:

$$S_n = S_0 \exp\left(-\frac{\xi^2}{2\Delta^2}\right)\exp\left(-\frac{\zeta^2}{2\Delta^2\epsilon^2}\right) \tag{10}$$

where $\xi = \sqrt{r^2 + r_s^2 - 2rr_s\cos\theta}$. For the sink term, we simply assume the adiabatic expansion of the source, namely, $S_{T_e} = -S_n$.

3. Simulation results

For the simulation parameters of R6F, we use $S_0 = 0.2, r_s = 0.8, \Delta = 0.1, \beta_i = \beta_e = 4 \times 10^{-3}, \delta = 110^{-2}, \epsilon = 1/3$. The mesh sizes are chosen as $513 \times 256 \times 128$. The initial profiles are shown in Fig.1.

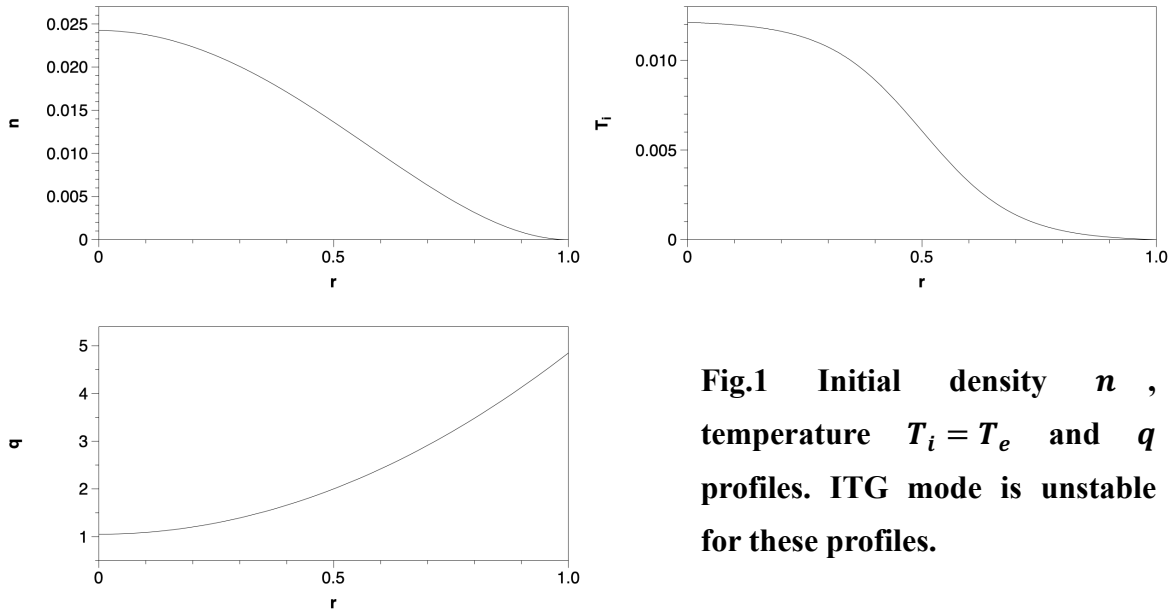

Fig.1 Initial density n, temperature $T_i = T_e$ and q profiles. ITG mode is unstable for these profiles.

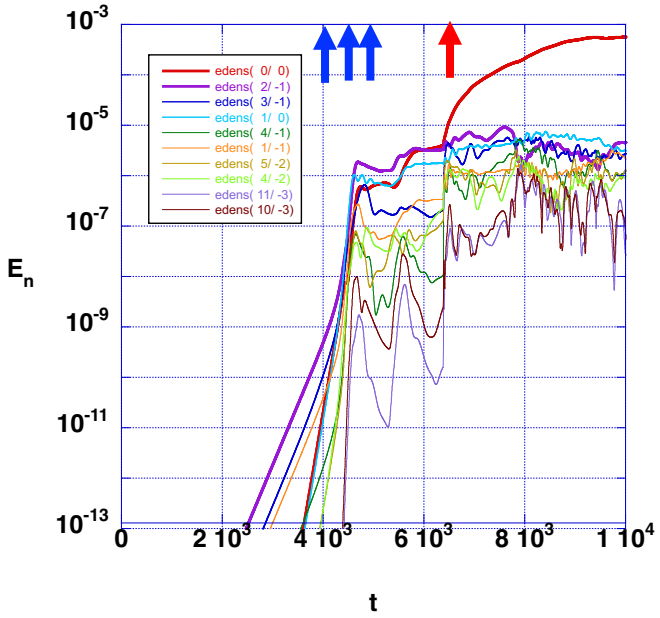

Fig.2 Time evolution of fluctuating density energy of each Fourier mode.

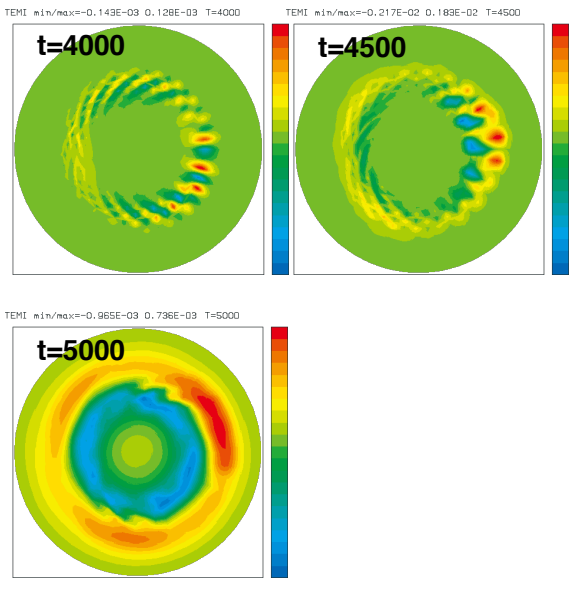

Fig.3 Contour plots of fluctuating ion temperature at ζ=0 plane.

Fig.2 shows the time evolution of fluctuating density energy of each Fourier mode which is given by the sixth term in Right Hand Side of eq. (8). At the early phase, ITG modes linearly grow up and the saturation is obtained at t=4300 due to the ion temperature profile relaxation. Then, the density source is applied at t=6400. Fig.3 shows the contour plots of fluctuating ion temperature on ζ=0 plane at t=4000, t=4500 and t=5000, respectively. It is clearly observed ITG mode structure at t=4000 and then the ion temperature relaxation occurs at t=5000. Fig.4 shows the contour plots of helical flux function, fluctuating density, total density and temperature at t=10000.

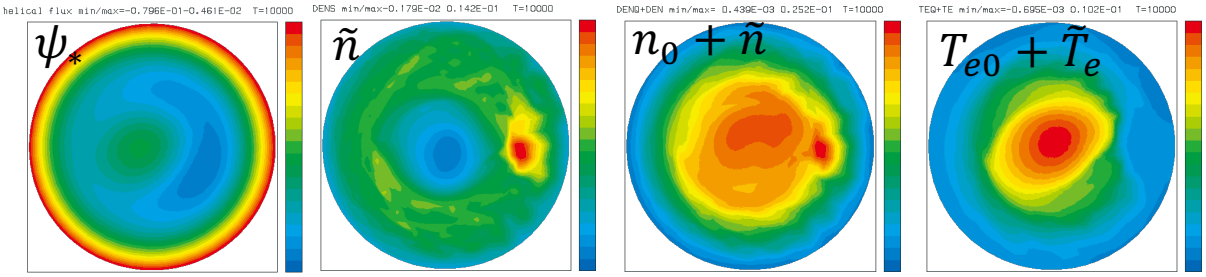

Fig.4 Contour plots of helical flux function, fluctuating density, total density and total temperature at t=10000.

It is seen that density source does not propagate homogeneously. This is because (2,1) magnetic island forms at r=0.5 which plays a role of barrier for density source propagation. It is clearly observed in the flux averaged total density and temperature shown in fig.5.

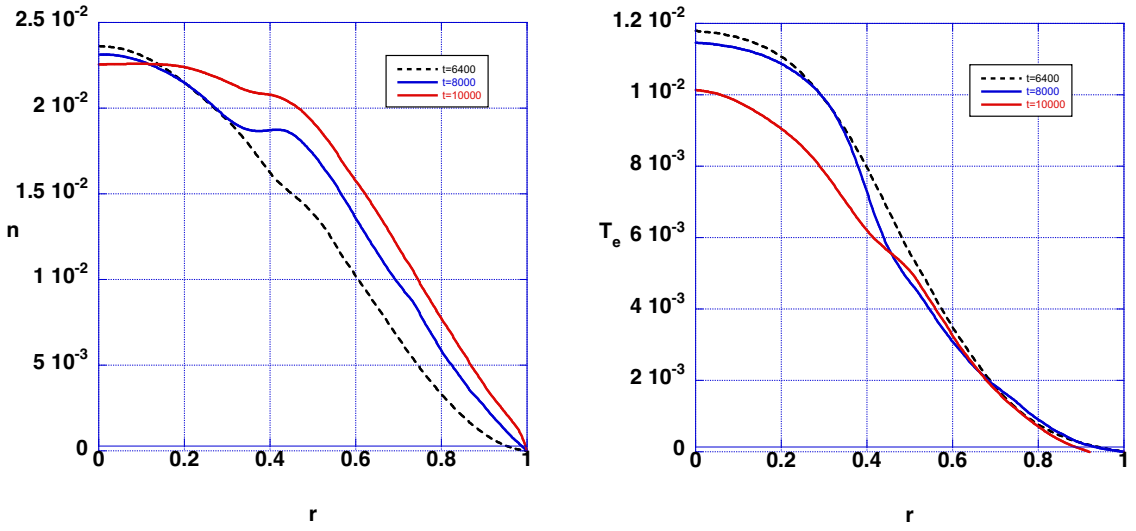

Fig.5 Flux averaged total density and temperature at t=6400(dashed), t=8000(blue), and t=10000(red), respectively.

The discontinuity point of radial derivative of the flux-averaged density appears around r=0.5 which indicates the propagation characteristics of density source is changed at this point. In addition, we observe the density hump on the mid-plane in Fig.4, however, it does not appear in the flux-averaged total density profile at t=10000.

4. Summary and discussion

We have developed 6-field drift reduced MHD model to investigate global particle transport with density source. The local density on the mid-plane shows density hump, however, for flux-averaged density profile, the hump does not form at the present time scale. We speculate that it is too short to equilibrate the density profile. In addition, well-developed turbulence (electron drift wave etc.) can not be captured for the present simulation. More long-time simulation run might be necessary. It is left for future work.

Acknowledgements

The author would like to thank Drs. N. Miyato, A. Matsuyama, N. Kasuya and T. Takizuka for useful comments. The computations were carried out on JFRS-1 supercomputer at IFERC-CSC and on SGI HPE8600 supercomputer at QST and JAEA.

References

[1] W. M. Tang, et. al., Phys. Rev. Lett. 35 (1975) 660-663.

[2] M. Yagi, et. al., ‘Revisit of ion-mixing mode transport’, 14th Japan-Korea Workshop on Modeling and Simulation of Magnetic Fusion Plasmas, 2019 June 27-28, RIAM Kyushu University.

[3] B. Coppi and C. Spight, Phys. Rev. Lett. 41 (1978) 551-554.

[4] R. Hazeltine and J. Meiss, Phys. Rep. 121 (1985) 1-164.

[5] M. Yagi and W. Horton, Phys. Plasmas 1 (1994) 2135-2139.

Study of turbulent transport in trapped electron and ion temperature gradient modes in high collision regime for tokamak plasmas

S. Toda, M. Nunami, and N. Kasuya[1]

National Institute for Fusion Science, Oroshi-cho 322-6, Toki, Gifu, 509-5292, Japan

[1]*Research Institute for Fusion Science, Kyushu University, Kasuga-koen 6-1, Kasuga, Fukuoka, Japan*

The purpose of this study is to quantify turbulent transport in toroidal plasmas. Microscopic plasma instabilities are studied using electromagnetic gyrokinetic simulations. Linear calculations are used to investigate the type of instability and to evaluate the conditions for instability excitation. The saturation level of the instability is determined from nonlinear calculations to obtain the turbulent transport value. The plasma experiments at the PLATO device at the Research Institute for Applied Mechanics, Kyushu University [1] have been started. The plasma profiles in the PLATO are predicted using the integrated code, the TASK code [2]. The gyrokinetic analysis have been performed for the plasma profile and magnetic field configuration which were predicted by the TASK, as an example in the PLATO. The instabilities are shown to be exited by the trapped electron mode (TEM) because of the increase of the density gradient [3] where the characteristic frequency is between the ion and electron bounce frequencies [4, 5] and ion temperature gradient (ITG) mode in the predicted parameter regions for the PLATO. Previously, an analytic model, the fluid-based model and the gyrofluid model for the ITG-TEM analysis have been reported. The local gyrokinetic simulation has been performed for the ITG-TEM plasmas. Although the global gyrokinetic codes have been developed and performed, a local gyrokinetic simulation using the model collision operators [6, 7] is performed in this study. First, the type of the instability and the condition under which the instability occurs are studied by the linear gyrokinetic simulations. Next, the nonlinear simulation demonstrates the time evolution of the electrostatic potential fluctuations. The results of the simulations obtained by using the Sugama collision operator [6] are compared with those by the Lenard-Bernstein collision operator [7]. In the previous studies, the reduced models are constructed in the adiabatic electron condition and the kinetic electron condition [8] for the ion temperature gradient (ITG) turbulence in helical plasmas. These reduced models, which are constructed by the linear simulation results, quickly reproduce the nonlinear simulation results for the turbulent transport, thus, these reduced models enable us to simulate the integrated (dynamical) transport simulation, when the turbulent transport is evaluated by the reduced models in the dynamical transport simulation [9]. The simulation study for the TEM and ITG mode plasmas in this article is the basis when the reduced models for the TEM and ITG mode turbulence in tokamak plasmas will be constructed.

The turbulence driven by microinstabilities for the predicted plasmas in the PLATO is studied. The plasma experiments at the PLATO device [1] have been started. The plasma profiles [2] predicted by the TASK code in the PLATO are used. Toroidal plasmas with concentric circular flux surfaces are studied. For simplicity, the profile of the safety factor, $q(\rho) = 1 + 2\rho^2$ is set. The detailed analysis for the safety factor in the PLATO has been performed [10]. In this study,

the GKV code [11] is used for the local flux tube gyrokinetic simulation. The normalized collision frequencies, ν_e^* and ν_i^* are shown as 0.22 and 8.8 at $\rho = 0.65$, respectively. Therefore, the electrons form the banana orbit and the ions do not. The normalized electron and ion radii are about $\rho_{\rm e}^* = 3.9 \times 10^{-4}$ and $\rho_{\rm i}^* = 6.5 \times 10^{-2}$ at $\rho = 0.65$, respectively. Therefore, the GKV code is performed in the unit of $R/L_{T_{\rm e}}$, $R/v_{\rm te}$ and $k_y\rho_{\rm e}$.

The linear gyrokinetic simulation is performed in tokamak plasmas. The linear simulation results using the Sugama (S) collision operator and the Lenard-Bernstein (LB) collision operator are compared. The dependences of the linear growth rate, γ on the normalized poloidal wavenumber, $k_y\rho_{\rm e}$ are studied at $\rho = 0.47, 0.65$ and 0.81. The real frequency, ω as the function of $k_y\rho_{\rm e}$ are also investigated. The instabilities predicted in this study are driven by the trapped electron mode (TEM) and the ion temperature gradient (ITG) mode at $\rho = 0.47$ and $\rho = 0.65$. The real frequency changes from the electron to ion diamagnetic drift motion direction at $\rho = 0.47$ and $\rho = 0.65$ when the poloidal wavenumber increases. The TEM is unstable, where the normalized electron plasma frequency is less than the unity [4, 5]. The phenomena such as the transition from the TEM to the ITG mode are obtained in the dependence of the real frequency on the poloidal wavenumber, specially at $\rho = 0.65$ using the S collision operator. The TEM mode is predicted to unstable at $\rho = 0.81$. Using the S collision operator, the ITG mode is unstable in the region $0.026 \leq k_{\rm y}\rho_{\rm e} < 0.100$ at $\rho = 0.47$ and in the region $0.030 \leq k_{\rm y}\rho_{\rm e} < 0.100$ at $\rho = 0.65$. On the other hand, the ITG mode is stable in these poloidal wavenumber regions, when the LB collision operator is used.

Nonlinear gyrokinetic analysis results are studied for the time evolutions of the squared turbulent potential fluctuation, $\mathcal{T}\left(=\Sigma_{\tilde{k}_x,\tilde{k}_y\neq 0}\left\langle|\tilde{\phi}_{\tilde{k}_x,\tilde{k}_y}|^2\right\rangle/2\right)$ and the squared zonal flow potential, $\mathcal{Z}\left(=\Sigma_{\tilde{k}_x,\tilde{k}_y=0}\left\langle|\tilde{\phi}_{\tilde{k}_x,\tilde{k}_y}|^2\right\rangle/2\right)$ at $\rho = 0.47$, $\rho = 0.65$ and $\rho = 0.81$, where $\tilde{\phi}$ is the electrostatic potential fluctuation. The electron and ion heat diffusivities are obtained as $29{\rm m}^2/{\rm s}$ and $32{\rm m}^2/{\rm s}$ at $\rho = 0.65$, respectively. The particle diffusivity is shown as $19{\rm m}^2/{\rm s}$. The nonlinear simulation using the S collision operator will be performed.

This work is partly supported by the NIFS Collaboration Research Programs, NIFS22KIST022 (Plasma Simulator), the JSPS KAKENHI Grant No. 21K03514 and the Collaborative Research Program of Research Institute for Applied Mechanics, Kyushu University, 2022FP-02.

[1] A. Fujisawa, *AIP Conference Proceedings* **1993**, 020211 (2018)
[2] N. Kasuya, The 16th Burning Plasma Simulation Initiative (BPSI) Meeting (2018)
[3] B. Coppi and G. Rewoldt, *Phys. Lett.* **49A**, 36 (1974)
[4] B. B. Kadomtsev and O. P. Pogutse, Reviews of Plasma Physics, edited by M. Leontovich (consultants Bureau, New York, 1970), Vol. 5
[5] W. M. Tang *et al.*, *Phys. Rev. Lett.* **35**, 660 (1975)
[6] H. Sugama, T. -H. Watanabe and M. Nunami, *Phys. Plasmas* **16**, 112503 (2009)
[7] A. Lenard and I. B. Bernstein, *Phys. Rev.* **112**, 1456 (1958)
[8] S. Toda *et al.*, *Phys. Plasmas* **26**, 012510 (2019)

[9] S. Toda, M. Nunami and H. Sugama, *Plasma Phys. Control. Fusion* **64**, 085001 (2022)
[10] S. Tomimatsu *et al.*, *Plasma and Fusion Research* **15**, 1403052 (2020)
[11] T. -H. Watanabe and H. Sugama, *Nucl. Fusion* **46**, 24 (2006)

Several Low-Cost Techniques for Global Plasma Simulation with Particle-in-Cell Model

T. Takizuka [1], K. Ibano [1], S. Togo [2]

[1] Graduate School of Engineering, Osaka University, Suita 565-0871, Japan
[2] Plasma Research Center, University of Tsukuba, Tsukuba 305-8577, Japan

Kinetic particle model is valuable even for global simulations of low-collisionality fusion plasmas, although the computational cost is very high. We have been proposed several techniques to lower the computational cost for global plasma simulations with Particle-in-Cell model; "Weighted Particle model" for hugely multiplying particle number, "Double Leap-Frog method" for larger time step, "Ingenious plasma simulation model" for longer spatial grid size, etc. Even when the above models are used, the numerical heating is unavoidable especially for smaller particle number per cell. Here we propose a "Numerical Heating Correction method" and "Increasing/Decreasing Particle Number techniques".

1. Introduction

Numerical simulations have been widely carried out for various fields of plasma science. Global plasma simulations, exceeding local simulations, are important especially for fusion plasma R&D. Since kinetic effects are essential in low-collisionality plasmas, the kinetic particle model is valuable even for global simulation [1]. The computational cost of the particle simulation, however, is very high. For example, a three-dimensional (3D) particle simulation of a tokamak plasma (volume $V_p \sim 10\,\mathrm{m}^3$ and time scale $\mathcal{T}_{sim} \sim 10\,\mathrm{ms}$) including the self-consistent electron dynamics needs large amounts of super-particle number $N_{tot} \sim 10^{13}$ and time steps $K_{step} \sim 10^8$ (grid size $\Delta \sim 1\,\mathrm{mm}$, particle number per cell $N_{cell} \sim 10^3$, and time step $\Delta t \sim 10^{-10}\mathrm{s}$). Resultant calculation steps become very huge $K_{cal} \sim 10^{24}$ (for operation per step $\sim 10^3$). Using 400 PFLOPS "Fugaku" system, a single run may require ~ 1 year.

To reduce the computational cost, the super-particle concept has been applied in the Particle-in-Cell (PIC) modeling. In the above tokamak plasma with electron density $n_e \sim 10^{19\text{-}20}/\mathrm{m}^3$, the real particle number $\mathcal{N}_{real} \sim 10^{20\text{-}21}$ is reduced to the super-particle number $N_{tot} \sim 10^{13}$. Since Coulomb collision nature is deformed in the PIC model, a "**binary collision model**" based on a Monte-Carlo technique with low cost was developed [2], and has been applied widely to the global plasma simulations.

When we study with the particle simulation the vapor shielding effect at the ELM or disruption event, large amount of impurities are emitted from the wall and the particle number is drastically increased. In order to suppress the corresponding increase of the super-particle number, a "**weighted particle model**" was introduced to the PIXY code and the computational cost was much reduced [3].

Leap-frog (LF) method is simple to follow the gyration motion of a charged particle with energy and magnetic moment conservation and accurate drift. The simulated Larmor radius, however, becomes very large for $\Omega\Delta t \gg 1$ (Ω is cyclotron frequency). If the LF method is applicable to large $\Omega\Delta t$ case, new particle simulation codes can be more easily developed, such as the PIXY of multi-species (electron, $H^+/D^+/T^+$, impurities) code, in which the same subroutine is utilized for all particle motions. We proposed therefore a "**double leap-frog method**" [4]. By repeating the LF steps doubly and adopting the averaged velocity to advance the particle position, the Larmor radius is kept real independently of the $\Omega\Delta t$ value.

When the size of a super-particle (or the grid size Δ) becomes much larger than the Debye length λ_D, the explosive heating called "finite grid instability" occurs with a growth rate γ of the order of plasma frequency ω_p, and decent simulation results are never obtained [5]. In a tokamak fusion plasma, λ_D is very short ~ 0.1–0.01 mm for $n_e \sim 10^{19\text{–}20}/\mathrm{m}^3$ and electron temperature $T_e \sim 10^{2\text{–}4}\,\mathrm{eV}$. This length is much shorter than a possible grid size $\Delta \sim 1\,\mathrm{mm}$ in a global simulation. We therefore proposed an "**ingenious plasma simulation model**" stably carried out even for the longer Δ [6,7]. An artificial

permittivity ε^* much greater than ε_0 (permittivity of free space) is introduced to the Poisson equation, $\nabla(\varepsilon^*\nabla\phi) = -\rho$ (ϕ is electrostatic potential and ρ is charge density), and λ_D^* is artificially elongated by $(\varepsilon^*/\varepsilon_0)^{1/2}$ times. A large-scale system can be treated with a reasonable number of spatial grids. A dielectric tensor is adopted for the 3D global simulation of tokamak plasmas in the cylindrical coordinates (R, θ, Z). A diagonal element $\varepsilon_{\theta\theta}$ for toroidal axis θ is set much larger than those for the poloidal plane, $\varepsilon_{RR} = \varepsilon_{ZZ} = \varepsilon^*$. Number of toroidal meshes N_θ can be reduced enough smaller than that of poloidal-plane meshes, N_R and N_Z, in comparison with $N_\theta > N_R, N_Z$ for the usual case of isotropic ε^*.

Even for $\Delta \sim \lambda_D^*$ of the "ingenious model", the numerical heating is unavoidable in the PIC modeling. This heating rate is in inverse proportion to the super-particle number per cell, N_{cell}. In spite of the large numerical heating risk, it is convenient to save $N_{cell} \sim 100$ for the reasonable computation cost of multi-dimensional particle simulation. The cost of the former 3D tokamak simulation ($V_p \sim 10\,\mathrm{m}^3$ and $\mathcal{T}_{sim} \sim 10\,\mathrm{ms}$) can be reduced much by the following numerical condition; $\Delta_{R,Z} \sim 2\,\mathrm{mm}$, $\Delta_\theta \sim 10\,\mathrm{mm}$, $\Delta t \sim 10^{-9}\,\mathrm{s}$, $N_{cell} \sim 100$, and $N_{tot} \sim 10^{10}$. Resultant run of $K_{cal} \sim 10^{20}$ requires ~ 1 day by 10 PFLOPS "Raijin" system. In the next section, we briefly review the numerical heating, and propose a "**numerical heating correction method**". In section 3, we also propose "**increasing/decreasing particle number techniques**".

2. Numerical heating correction method [8]

In the PIC model, the electric field $\boldsymbol{E}$ is recorded at the grid points, and nonphysical aliases of $\boldsymbol{E}$ arise on an off-grid-point particle. This aliasing effect causes the finite-grid instability for $\Delta \gg \lambda_D$ (or λ_D^*). Even for $\Delta \sim \lambda_D^*$, the aliasing $\boldsymbol{E}$ noise suffers the electron velocity parallel to the magnetic field $\boldsymbol{B}$, and causes the numerical heating in the parallel component of electron energy. Major source of the numerical-heating field is of the short wave-length statistical fluctuation, whose amplitude is in inverse proportion to $(N_{cell})^{1/2}$; $e\delta E\Delta/T_e \sim f_A(\Delta/\lambda_D^*)^2/(N_{cell})^{1/2}$. Aliasing factor f_A can be ~0.1 for the linear-shape PIC. Electron velocity is diffused by this noise field, and the diffusion coefficient in the velocity space is $D_v \sim (e\delta E/m_e)^2\,\Delta t_{eff}$, where $\Delta t_{eff} \sim \{4(\Delta/v_{te})^2 + \Delta t^2\}^{1/2}$ is the decorrelation time (v_{te} is electron thermal speed). The numerical heating rate is then evaluated as $\gamma_N\ (\equiv \mathrm{d}\ln T_e/\mathrm{d}t) \sim D_v/v_{te}^2 \sim \omega_p^* f_A^2(\Delta/\lambda_D^*)^3/N_{cell}$ for $\Delta t < \Delta/v_{te}$ [1]. Simulation result by Ueda et al. was $\gamma_N \approx (1/1600)\,\omega_p(\Delta/\lambda_D)^3/N_{cell}$ in a periodic 1D system [9]. This unphysical increase of T_e becomes quite large for a confined plasma, and interrupts a long-time scale global simulation. The higher-order shaping of a super-particle (quadratic spline and cubic spline) can reduce the heating rate [10], but still cannot fully suppress the numerical heating.

Because the linear spline (PIC) is simple for the multi-dimension system and is preferable for the boundary treatment in the open system, we do not adopt the higher-order shaping while we consider a correction method of the numerical heating in the PIC simulation. Complete suppression of the numerical heating is accomplished by the following correction procedures.

Correction procedures for every time step

(i) Simply smoothed electric field parallel to $\boldsymbol{B}$, $\boldsymbol{E}_\parallel = (\boldsymbol{E}\cdot\boldsymbol{B})\boldsymbol{B}/B^2$, is calculated at a grid point j;

$$\langle \boldsymbol{E}_\parallel{}^j \rangle = (\boldsymbol{E}_\parallel{}^{j+1} + 2\boldsymbol{E}_\parallel{}^j + \boldsymbol{E}_\parallel{}^{j-1})/4 \qquad (1)$$

Fluctuation energy of "smoothed" field $\Sigma_j \langle \boldsymbol{E}_\parallel{}^j \rangle^2$ becomes small by ~1/3 compared with the "original" fluctuation energy $\Sigma_j (\boldsymbol{E}_\parallel{}^j)^2$.

(ii) Each electron velocity $\boldsymbol{v}(t)$ is advanced to $\boldsymbol{v}^*(t+\Delta t)$ with the "original" $\boldsymbol{E}$. The perpendicular component is determined, $\boldsymbol{v}_\perp(t+\Delta t) = \boldsymbol{v}^*_\perp(t+\Delta t)$, at this step.

(iii) Each electron velocity $\boldsymbol{v}_\parallel(t)$ parallel to $\boldsymbol{B}$ is advanced to $\boldsymbol{v}_{\#\parallel}(t+\Delta t)$ with the "smoothed" $\langle \boldsymbol{E}_\parallel \rangle$;

$$\boldsymbol{v}_\#(t+\Delta t) = \boldsymbol{v}^*(t+\Delta t) - (e/m_e)\,(\langle \boldsymbol{E}_\parallel \rangle - \boldsymbol{E}_\parallel)\,\Delta t \qquad (2)$$

$$\boldsymbol{v}_{\#\parallel}(t+\Delta t) = \{\boldsymbol{v}_\#(t+\Delta t)\cdot\boldsymbol{B}\}\boldsymbol{B}/B^2 \qquad (3)$$

(iv) Total energy increments (including ion contribution), ΔW_* and $\Delta W_\#$, are calculated for the "original" $\boldsymbol{E}$ step (ii) and for the "smoothed" $\langle \boldsymbol{E}_{||} \rangle$ step (iii), respectively.

(v) Input and output powers in the total system (hot particle supply, ohmic heating, external heating, fusion power, convection/conduction loss to the wall, radiation loss, atomic & molecular reaction loss etc.) are counted. Physical heating power P_{in} should be accurately evaluated. Physical energy balance is then known; $\Delta W_0 = (P_{in} - P_{loss})\,\Delta t$. After that numerical heating energies, ΔW_{N*} and $\Delta W_{N\#}$, are calculated;

$$\Delta W_{N*,\#} = \Delta W_{*,\#} - \Delta W_0 \qquad (\Delta W_{N*} > \Delta W_{N\#}) \tag{4}$$

(vi) Assuming the numerical heating comes from only electrons, the parallel electron energy is cooled by keeping the direction of the parallel velocity as

$$v_{||}^{\,2} = v_{*||}^{\,2} - (v_{*||}^{\,2} - v_{\#||}^{\,2})\,\Delta W_{N*}/(\Delta W_{N*} - \Delta W_{N\#}) \tag{5}$$

$$\boldsymbol{v}_{||}(t+\Delta t) = (v_{||}^{\,2}/v_{\#||}^{\,2})^{1/2}\,\boldsymbol{v}_{\#||}(t+\Delta t) \tag{6}$$

Total excess energy is fully removed in the entire system. Note that a simple cooling w/o the "smoothed" $\langle \boldsymbol{E}_{||} \rangle$ procedures causes the numerical heat transport.

(vii) Spatial position is moved (LF method); $\boldsymbol{r}(t+3\Delta t/2) = \boldsymbol{r}(t+\Delta t/2) + \boldsymbol{v}(t+\Delta t)\,\Delta t$.

(viii) Collisional change is added by using a binary collision model (Takizuka-Abe [1]).

Complete suppression of the numerical heating in the entire system can be accomplished by the above correction method.

3. Increasing/decreasing particle number techniques

In order to perform a global plasma simulation with a convenient number of super-particles, it is efficient to vary arbitrarily the particle number during a simulation run. A long-duration simulation could be carried out with $N_{cell} \sim 10^2$, and an accurate result could be obtained in a short period with $N_{cell} \sim 10^3$. Further reduction of $N_{cell} \sim 10$ is desirable in the pre-simulation to obtain an initial equilibrium state. Previous PARASOL 2D simulation, the particle number was multiplied by 10 times at once from the pre-simulation (w/o self-consistent $\boldsymbol{E}$) to the full simulation [11]. Now we propose "increasing/decreasing particle number techniques", where we employ the "doubling/halving number processes".

Figure 1 shows the temporal evolution of the total particle number in the system, N_{tot}. During the increasing/decreasing phase, N_{tot} is doubled/halved at a time step. A short plateau ($\sim 10^2\,\Delta t$) is put after a doubling/halving process to suppress the unexpected fluctuation induced by this process. It takes seven doubling/halving processes ($2^7 = 128$) and $\sim 10^3\,\Delta t$ duration for the increasing/decreasing of N_{tot} by hundred-fold/one-hundredth. A certain simulation result is obtained in a long plateau ($>10^3\,\Delta t$). During the plateaus, physical increase/decrease of N_{tot} is naturally allowed.

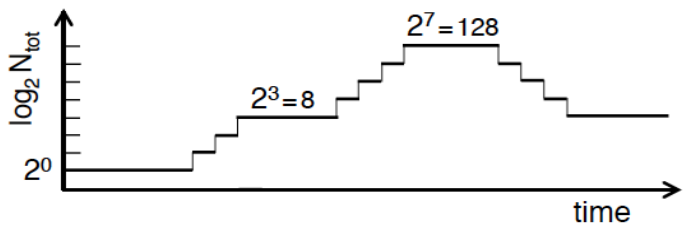

Fig. 1 Temporal evolution of total particle number in the system, N_{tot}. Series of doubling/halving processes, and short/long plateaus are seen.

"Doubling process"

A super-particle with ($\boldsymbol{r}_0$, $\boldsymbol{v}_0$, w_0) is doubled to two super-particles with ($\boldsymbol{r}_1$, $\boldsymbol{v}_1$, w_1) and ($\boldsymbol{r}_2$, $\boldsymbol{v}_2$, w_2), respectively. The weight of doubled particle is half of the first particle, $w_1 = w_2 = w_0/2$. Their new velocities and positions are given as

$$\boldsymbol{v}_1 = \boldsymbol{v}_0 + (\boldsymbol{v}_0 + \boldsymbol{v}_1) \times \boldsymbol{\Theta}_p\,, \quad \boldsymbol{r}_1 = \boldsymbol{r}_0 + \boldsymbol{v}_1 \Delta t_p \tag{7}$$

$$\boldsymbol{v}_2 = \boldsymbol{v}_0 - (\boldsymbol{v}_0 + \boldsymbol{v}_2) \times \boldsymbol{\Theta}_p\,, \quad \boldsymbol{r}_2 = \boldsymbol{r}_0 - \boldsymbol{v}_0 \Delta t_p \tag{8}$$

where $\boldsymbol{\Theta}_p = \boldsymbol{\Omega}\Delta t_p/2$ and $(\boldsymbol{B}\cdot\boldsymbol{v}_0)\Delta t_p/B \sim \Delta$. Here the forward LF method, Eq. (7), and backward LF method, Eq. (8), are utilized to separate the spatial positions of doubled particles. A binary collision between $\boldsymbol{v}_1$ and $\boldsymbol{v}_2$ takes place with a scattering angle ~ $\pi/4$. The energy is conserved before and after a doubling process. Particle diffusion along $\boldsymbol{B}$ is naturally described here to reduce the source of numerical-heating $\boldsymbol{E}$ of the short wave-length statistical fluctuation.

"Halving process"

Two super-particles with ($\boldsymbol{r}_a$, $\boldsymbol{v}_a$, w_a) and ($\boldsymbol{r}_b$, $\boldsymbol{v}_b$, w_b), respectively, nearby are chosen as a pair. One remaining particle is selected, a or b (hereafter "a" for simplicity). The position $\boldsymbol{r}_a$ and parallel velocity $\boldsymbol{v}_{a||}$ are taken over by the new super-particle, $\boldsymbol{r}_1 = \boldsymbol{r}_a$ and $\boldsymbol{v}_{1||} = \boldsymbol{v}_{a||}$. The weight of the new particle is $w_1 = w_a + w_b$. Although the momentum is not conserved, $w_1\boldsymbol{v}_1 \neq w_a\boldsymbol{v}_a + w_b\boldsymbol{v}_b$, the energy conservation is maintained by modifying the perpendicular velocity $\boldsymbol{v}_{1\perp}$ as

$$\boldsymbol{v}_{1\perp}^2 = (w_a\boldsymbol{v}_a^2 + w_b\boldsymbol{v}_b^2)/(w_a + w_b) - \boldsymbol{v}_{1||}^2 \tag{9}$$

$$\boldsymbol{v}_{1\perp} = (\boldsymbol{v}_{1\perp}^2/\boldsymbol{v}_{a\perp}^2)^{1/2}\,\boldsymbol{v}_{a\perp} \tag{10}$$

The momentum conservation is also possible, if necessary, by applying the cell-average correction in the "**weighted-particle collision model**" [12]. Halving pair particles are chosen mainly in the same cell, but the inter-cell pair is allowed. Last one particle not paired in the system if exist is 50%-life ($w_1 = 2w_a$) or 50%-death ($w_1 = 0$).

4. Summary

Kinetic particle model is valuable even for global simulations of low-collisionality fusion plasmas, although the computational cost is very high. We have been proposed several techniques to lower the computational cost for global plasma simulations with Particle-in-Cell model; "weighted particle model" for hugely multiplying particle number [3], "double leap-frog method" for larger time step [4], "ingenious plasma simulation model" for longer spatial grid size [6,7], etc. Even when the above models are used, the numerical heating is unavoidable especially for smaller particle number. A "numerical heating correction method" is proposed for longer time-scale global plasma simulation with smaller particle number [8]. "Increasing/decreasing particle number techniques" are also proposed for the efficient simulation with arbitrary particle number. These low-cost techniques will be applied and tested during our development of the PIXY code (multi-dimensional PIXY for the mirror confinement system) in the near future.

References

[1] T. Takizuka, Plasma Phys. Control. Fusion **59**, 034008 (2017).
[2] T. Takizuka, H. Abe, J. Comput. Phys. **25**, 205 (1977).
[3] K. Ibano, Y. Kikuchi, S. Togo, Y. Ueda, T. Takizuka, Nucl. Fusion **59**, 076001 (2019).
[4] T. Takizuka, K. Ibano, S. Togo, Plasma Fusion Res. **16**, 1203100 (2021).
[5] R.W. Hockney, J.W. Eastwood, *Computer Simulation Using Particles* (New York, McGraw-Hill, 1981).
[6] T. Takizuka, K. Ibano, M. Yagi, Plasma Fusion Res. **13**, 1203088 (2018).
[7] T. Takizuka, K. Ibano, M. Yagi, Plasma Fusion Res. **14**, 1203091 (2019).
[8] T. Takizuka, K. Ibano, S. Togo, "Correction of Numerical Heating in Global Plasma Simulation with Particle-in-Cell Model", presented at 27th Int. Conf. Numerical Simulation of Plasmas (Nagoya; Online, 2022), P-6; https://www.p.phys.nagoya-u.ac.jp/27thicnsp/program.html .
[9] H. Ueda, Y. Omura, H. Matsumoto, T. Okuzawa, Comput. Phys. Commun. **79**, 249 (1994).
[10] H. Abe, N. Sakairi, R. Itatani, J. Comput. Phys. **63**, 247 (1986).
[11] T. Takizuka, K. Shimizu, N. Hayashi, M. Hosokawa, M. Yagi, Nucl. Fusion **49**, 075038 (2009).
[12] A. Tanaka, K. Ibano, T. Takizuka, Y. Ueda, Contrib. Plasma Phys. **58**, 451 (2018).

磁化プラズマにおける巨視的構造診断のためのシミュレーション

Global structure and its diagnostic simulation in magnetized plasmas

N. Kasuya
RIAM, Kyushu University, Kasuga, Fukuoka 816-8580, Japan
E-mail: kasuya@riam.kyushu-u.ac.jp

1. Introduction

Plasma turbulence has large effects on particle and heat transport in magnetically-confined fusion plasmas, and it is important to clarify its 3-D feature in real magnetic geometries in torus experiments, because various global and meso-scale structures are formed. Synthetic diagnostics use simulation data to represent experimental measurements by simulating measurement signals [1]. Numerical simulations can show global features of mean profile modifications and fluctuation excitations, and quantitative comparison between experiments and simulations is possible. Several kinds of simulations use different models, depending on the simulation targets, so comparison between models is also important to capture various characteristics in magnetized plasmas. In addition, combination of multiple simulation results can give complex plasma characteristics including several physical mechanisms. We have carried out some numerical diagnostics [2,3], and then newly develop these routines into an integrated numerical diagnostic platform for turbulence and structural formation analyses, which can be applied to multiple simulation data that have different data formats [4]. The concept of the integrated diagnostic simulator is explained and is applied to observations of a formed mean profile and fluctuation distribution in real magnetic geometries of fusion devices here. Effectiveness of this framework is shown for detecting global features by analyzing several kinds of numerical simulation data.

2. Integrated turbulence diagnostic simulator

The integrated turbulence diagnostic simulator (iTDS) is a framework for making global analyses in real magnetic geometries of fusion devices [4]. iTDS connects global simulations and experimental observations. Various analysis routines for several experimental diagnostics are developed on this platform. The analysis consists of the following processes;

i) 3-D simulation of plasma instabilities and transport
ii) Plasma device parameter set and adjustment of the data format (if necessary)
iii) Simulation to obtain signals by experimental diagnostics

In process i), several codes can be used to obtain 3-D plasma profiles and time evolution of fluctuations. Global codes are used for calculations in torus plasma geometries. In general, particular models do not always include all the necessary quantities, so lacked information is supplemented with other calculation or assumption, if necessary in process ii). In addition, spatial coordinates in simulation codes may be different with ones used for numerical measurement, so data transfer is necessary in that case. Data mapping to the common format is often used, but here we introduce the object-oriented method in accordance with each data format to gain the maximum information. The data transfer is limited to the minimum. Then the numerical measurements are carried out in process iii). The basic component to capture 3-D dynamics from simulation data is extracting the local value at the arbitrary position from discreet data by interpolation. The combination of this basic routine can give multi-point observation along a line of the sight of each diagnostic. Here the focus is mainly set on a geometric effect from magnetic configurations. Applications of iTDS is explained in the followings to show mean profile and fluctuation measurements in torus experimental devices.

3. Steady profile measurement

Heavy ion beam probe (HIBP) is powerful diagnostic to give information of several kinds of quantities [5]. Single trajectory of the detected ion can be selected with given injection and detection conditions, which determines the observation position. Plasma fluctuations and electromagnetic fields inside the plasma can be measured simultaneously without disturbing the plasma. Calculation of 3-D trajectory of heavy ions, including non-circular plasma shape and experimental arrangement of diagnostics, is carried out by synthetic HIBP (sHIBP) in iTDS for LHD [6]. Mean radial Φ_0 and 3-D perturbation Φ_1 profiles of the potential are included in the 3-D magnetic configurations. The 3-D variation of the potential is calculated by global drift kinetic code FORTEC-3D, which is given by the neoclassical process [7]. This 3-D variation is predicted to affect the impurity neoclassical transport. The observation points depend on the injection conditions of the heavy ions, so the profile scan can be made. The deviation of the potential values from the radial mean comes from Φ_1, which depends on the observation point. For assessment of observability in the experiment, the intensity of the detected beam is important, which is also evaluated in sHIBP. Here beam attenuation is calculated by using ionization cross sections from Lotz's empirical formula [8]. The detected beam intensity is predicted to be larger than the noise level given by the detector.

4. Fluctuation measurement

Phase Contrast Imaging (PCI) utilizes the laser scattering by density fluctuations [9]. Interference between scatted beam and non-scatter beam gives the fluctuation image on the imaging plate. The line integration is obtained as the observed signal. Local information is needed to be deduced from the line integration, and in helical plasma variation of the magnetic field direction can be used for the separation, because the fluctuation is elongated along the field line at each position [10]. Synthetic PCI (sPCI) is carried out to make this separation process of the spectrum using 3-D fluctuation data in iTDS. A fluctuation pattern is obtained by gyrokinetic simulation in LHD [11], and the magnetic shear method is applied for comparison with LHD experimental result [3]. Turbulence analyses using a torus global simulation are also carried out.

5. Sumarry

Synthetic diagnostics, which give simulations of experimental signals by using global simulation data of 3-D plasma turbulence, are carried out for precise comparison between experiments and simulations. iTDS has been developed as the platform for synthetic diagnostics by including 3-D magnetic geometry. Several kinds of diagnostics as HIBP and PCI provide measurements for wide range of plasmas. Diagnostics using plasma waves, and measurements of plasma distribution function are also useful, which are future tasks.

Acknowledgements

This work was partially supported by JSPS KAKENHI JP17H06089, JP20K03905, and the collaboration program of NIFS (NIFS22KIST029) and of RIAM of Kyushu University. Some calculations were carried out using the JFRS-1 supercomputer system at IFERC-CSC in QST and Plasma Simulator supercomputer system in NIFS.

References

[1] C. Holland, *et al.*, Phys. Plasmas **16** (2009) 052301.

[2] N. Kasuya, *et al.*, Plasma Sci. Tech. **13** (2011) 326.
[3] N. Kasuya, *et al.*, Nucl. Fusion **58** (2018) 106033.
[4] N. Kasuya, *et al.*, Proc. BPSI meeting (2022) PA-5.
[5] T. Ido, *et al.*, Rev. Sci. Instrum. **77** (2006) 10F523.
[6] R. Yoshihara, *et al.*, BPSI meeting (2023) PA-5.
[7] K. Fujita, *et al*., Nucl. Fusion **61** (2021) 086025.
[8] W. Lotz, Astrophys. J., Suppl. Ser. **14** (1967) 207.
[9] H. Weisen, Rev. Sci. Instrum. **59** (1988) 1544.
[10] K. Tanaka, *et al.*, Rev. Sci. Instrum. **79** (2008) 10E702.
[11] M. Nunami, *et al.*, Phys. Plasmas **19** (2012) 042504.

Carbon impurity modeling with the superstage model in TASK/TX

M. Honda, A. Matsuyama* and Y. Homma*

Kyoto University, Nishikyo-ku, Kyoto 615-8530 Japan

**National Institutes for Quantum Science and Technology, Rokkasho, Aomori 039-3212 Japan*

TASK/TX features and its extension with impurities

We are developing a fluid-type transport code TASK/TX [1,2] for simulating the evolution of physical quantities in torus plasmas. Unlike the diffusion-type equations, which are the governing equations of conventional transport codes, TASK/TX is transformed into an equation system that focuses on transport phenomena by taking a drift ordering for the two-fluid equation system. Furthermore, by taking a magnetic surface average, it becomes a one-dimensional fluid equation system. Also, in order to handle neoclassical transport self-consistently, it solves the $\left(1, \boldsymbol{v}, \frac{1}{2}v^2, \frac{1}{2}v^2\boldsymbol{v}\right)$ moment equations of the kinetic equation up to the heat flux order, which is not usually handled in the two-fluid equation system. TASK/TX is characterized by self-consistency between physical quantities, and thanks to its characteristics, the quasi-neutrality condition or the non-ambipolar condition are not imposed, which are the usual assumptions in conventional transport codes.

Recently, TASK/TX has been extended to handle impurities. To verify whether it works with impurities, we conducted a check of ambipolar transport in both the Matrix Inversion, which has been updated with a fully linearized collision operator implemented [3], and TASK/TX. Resultantly, it was confirmed that ambipolarity was held for both codes and also both results were in good agreement.

Superstage modeling in TASK/TX

As a major difference from hydrogen isotopes as bulk ions, impurities can exist in multiple charge states within the plasma. Carbon impurities are often assumed to be in the fully ionized hexavalent state, but this assumption may not always be valid in the edge

region. Also, assuming that the walls and divertor surfaces are made of carbon, physical and chemical sputterings caused by ions colliding with them, reflection and pumping of impurities at the divertor surfaces, and impurity injection are possible sources and sinks that should be considered, but in any case, impurities enter the plasma as neutral particles. Therefore, to model impurity sources appropriately, it is necessary to consider the multi-stage ionization process from neutral state to fully ionized state and the charge exchange process. So far, impurities have been able to handle only one charge state in TASK/TX, so impurity particle source modeling was also incomplete. By introducing the super-stage model [4], it has become possible to easily take into account the effects of the multicharge states from neutral carbon supply to full ionization. Solid lines in figure 1 show the time evolution of the carbon densities of each valence and dashed lines shows the time evolution of the densities, assuming that each valence takes a quasi-equilibrium state and grouping all charge states of carbon into one superstage carbon. In the figure, even when superstaged, C^{+6} converges to the same density as when the reaction rate equations were solved for all charge states, after a time longer than 10^{-3} second. In other words, since carbon is ionized from neutral to full ionization state within the time step width normally used in TASK/TX, the application of the superstage model that treats 0-5 valence carbon as pseudo neutral carbon is shown to be valid in the transport process that TASK/TX focuses on.

References

[1] M. Honda and A. Fukuyama, J. Comput. Phys. **227**, 2808 (2008).

[2] M. Honda and A. Fukuyama, Comput. Phys. Commun. **208**, 117 (2016).

[3] M. Honda, Phys. Plasmas **21**, 092508 (2014).

[4] A. Foster, *On the Behaviour and Radiating Properties of Heavy Elements in Fusion Plasmas*, PhD thesis, University of Strathclyde (2008).

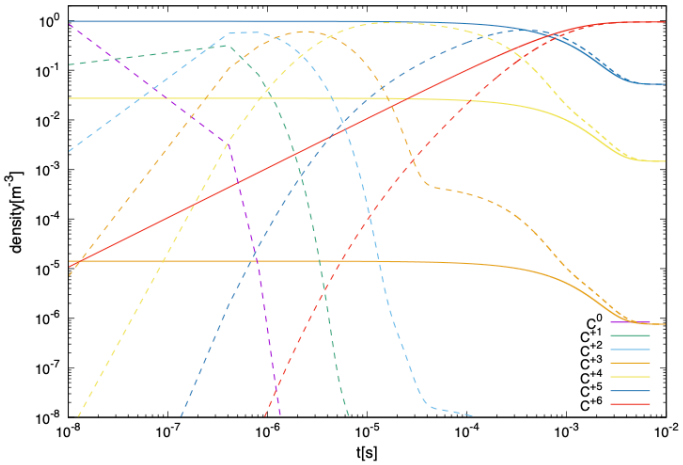

Fig. 1: At T_e = 200 eV, solid lines represent the time evolution of the densities of each valence when carbon impurities from 0 to 5 valence are superstaged, and dashed lines represent the time evolution of the densities of each valence when the reaction rate equations are solved.

Analysis of turbulent particle fluxes by using 5-field RMHD code in torus plasmas

H. Todoroki[1], N. Kasuya[1,2], M. Yagi[3]
IGSES, Kyushu Univ.[1], RIAM, Kyushu Univ.[2], QST[3]

1. Introduction

Fueling to the core plasma is one of the key issues to maintain a high fusion reaction rate in fusion plasmas. Pellet injection is promising as a fueling method because, in principle, it can efficiently supply particles to the core plasma. In fueling by pellet injection, a high-density region is created near the plasma edge due to pellet ablation, resulting in a density distribution with an inversed hump-shaped gradient in the radial direction. In the previous study [1], inversed density gradients are known to produce turbulent particle pinch. Furthermore, it is necessary to understand the transport mechanisms that are not only limited to local models but are also valid in global models.

In order to elucidate the mechanism of the particle pinch effect, which is effective in fueling to the plasma center by pellet injection into the fusion plasma, we perform turbulence simulations with particle transport by introducing a distribution with an inversed density gradient near the plasma edge. Particle convective transport is evaluated to clarify the time evolutions of the excited instabilities, when an inversed density gradient is introduced into tokamak plasmas.

2. Numerical model

Reduced MHD code R5F [2] is used for the simulation. The R5F code is a global simulation code using a 5-field reduced MHD model with neoclassical viscous effects. In this model, there are five variables to be solved: the potential ϕ, the vector potential parallel to the magnetic field A, parallel velocity V, electron density N, electron temperature T_e. For these five fields, the vorticity equation, Ohm's law, the parallel ion momentum equation, continuity equation, and the electron temperature evolution equations are used to solve the time evolution in 3-D space [3]. Each variable is normalized by using the minor radius in the spatial scales and the poloidal Alfven time in the temporal scales. The following tokamak plasma parameters are used for the simulations; major radius $R = 1.5\ m$, minor radius $a = 0.5\ m$, plasma beta $\beta = 10^{-2}$, normalized ion skin depth $\delta = 10^{-2}$. The inversed density gradient near the plasma edge due to pellet injection is given with the density source peak (density intensity S_{amp}) initially at the radial position $r = r_s$ as

$$N_{EQ} = N_0 + S_{amp} \exp\left(-\frac{(r-r_s)^2}{2\Delta^2}\right).$$

3. Linear phase results

In this study, we analyzed the cases with the initial density profiles for source density intensities of $S_{amp} = 1.0$ and 1.5, and source locations of $r_s = 0.8$. Figure 1 shows the initial density and safety factor profiles. We call the region of positive and negative density gradients near the position $r = r_s$ the inversed and normal gradient regions, respectively. As shown by the dashed lines in Fig. 1, there are resonant modes, for example, $(m,n) = (-25,8)$ and $(-36,14)$ in the normal and inversed gradient regions, where m and

n are the poloidal and toroidal mode numbers, respectively. Linear instabilities with ballooning structures localized at the low field side are excited. Direction and magnitude of the particle fluxes induced by these modes are evaluated. Figure 2(a) shows the radial profile of particle fluxes, whose magnification in the inversed gradient region is shown in Fig. 2(b). In Figure 2(a), the $n = 8$ component, which is strongly excited in the normal gradient region, is dominant overall to drive an outward particle flux. On the other hand, Fig. 2(b) shows that there is contributor to induce an inward particle flux in the inversed gradient region.

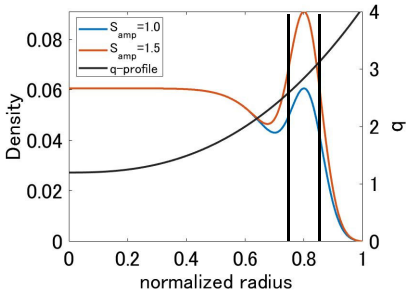

Fig.1 Initial density profiles with $S_{amp} = 1.0$ and 1.5. The safety factor profile is also shown.

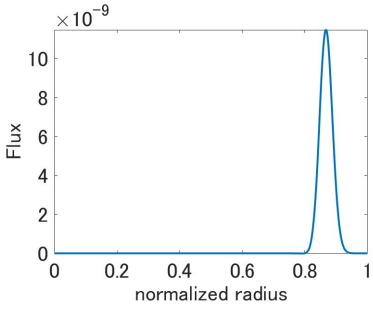

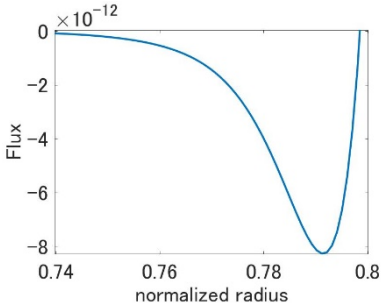

Fig.2 (a) Radial profile of particle fluxes in the linear phase at t = 65. The magnification of the inversed gradient region is also shown in (b).

The mode excited in the negative density gradient region is the resistive electron drift wave mode, and the dependence of its particle pinch effect on the density gradient is evaluated. Figure 3 shows the results of calculation for the linear growth rate in the inversed gradient region (ρ = 0.76) using electron drift wave mode theory. An instability boundary exists at the density gradient length $L_n \sim -8$. The turbulence simulations with $S_{amp} = 1.0$ and 1.5 have $L_n = -8$ and -13 in the negative gradient region, respectively, so it is consistent that the case with $S_{amp} = 1.5$ is more unstable to excite the electronic drift wave modes, though the case with $S_{amp} = 1.0$ is less unstable. Therefore, the time evolutions of the mode are also different to each other. The $n = 14$ component is excited in the inversed gradient region as the electron drift wave mode, and its particle flux increases in time in the unstable case with $S_{amp} = 1.5$, but is decreased in the stable case with $S_{amp} = 1.0$ as in Fig. 4, where the particle flux by the resonant mode with $(m, n) = (-36,14)$ in the inversed gradient region is shown. The unstable mode induces the particle pinch, which increases with the larger density gradient.

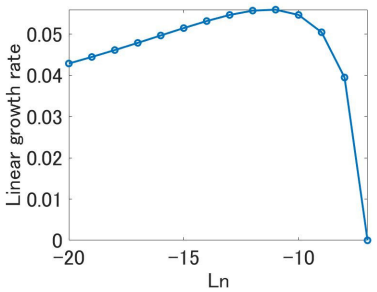

Fig.3 Linear growth rate in the reversed gradient region ($\rho = 0.76$).

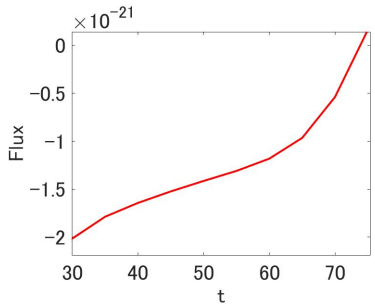

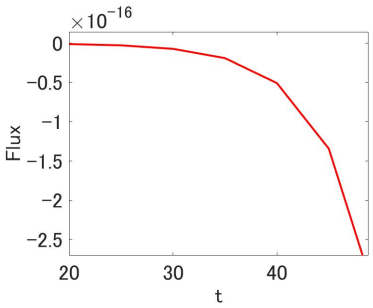

Fig.4 Time evolutions of the particle fluxes by the $(-36,14)$ mode with (a) $S_{amp} = 1.0$, and (b) 1.5.

4. Nonlinear phase results

The effects of profile relaxation and existence of multiple types of instabilities are shown in the nonlinear phase of the calculation. Figure 5 shows the mode amplitude profiles (a) just before the nonlinear phase (t = 50) and (b) during the nonlinear saturation phase (t = 120). At t = 50, the ballooning mode with $n = 8$ is dominant, while at t = 120, a tearing mode with $n = 1$ is dominant. The higher wavenumber components shown in Fig. 5(a) form the ballooning structure localized on the low field side, and in the nonlinear phase the modes spread radially to flatten the background pressure profile. This flattened profile makes the ballooning modes to be stable, and the mode intensities are decreased as in Fig. 5(b). The tearing instability grows near the rational surface with $q = 3$, and then in the nonlinear saturation phase becomes dominant.

Next, we evaluate the particle fluxes at the radial position where the ballooning and tearing modes exist. Figures 6(a-c) show the particle fluxes at ρ = 0.6, 0.73, and 0.83, which are corresponding to the positions of the rational surface with $q = m/n = 2, 2.5$, and 3, respectively. In Fig. 6(c), the contribution to outward particle flux from the ballooning mode is large in the linear phase, sharply increases just in the nonlinear saturation phase, and saturates with the relaxation of the background density profile. Figures 6(b) shows that the inward particle flux in the negative gradient region increases in the linear phase, keep increasing after the profile relaxation in the normal gradient region. The increase even in the nonlinear phase suggests that the contribution from the low-wavenumber components, including the tearing mode, exists in that phase.

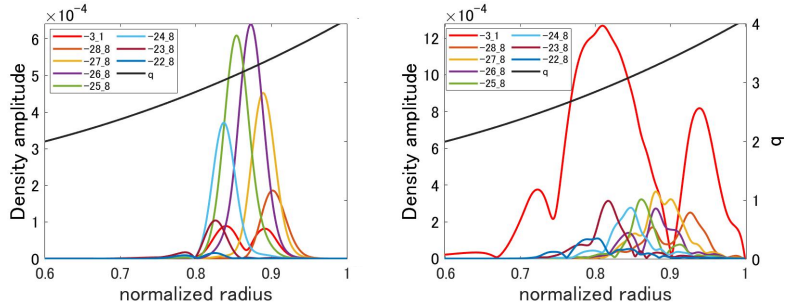

Fig.5 Mode structures of the excited modes (a) just before the nonlinear phase at t = 50, and (b) in the nonlinear phase at t=120. The mode amplitudes of the density are shown.

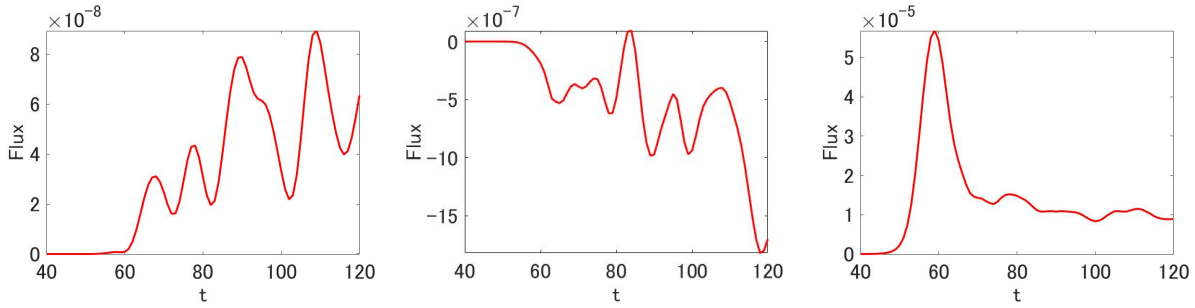

Fig.6 Time evolutions of the particle flux at radial positions ρ = (a) 0.6, (b) 0.73, (c) 0.83.

5. Conclusion

The R5F code was used to evaluate turbulent particle transport in a global simulation. The effect of the negative density gradient was investigated by introducing a density profile with an inversed density gradient near the plasma edge. Outward particle fluxes in the normal gradient region are dominant, and the evolution of the density profile is largely determined by this outward transport. On the other hand, inward particle fluxes are also observed in the inversed gradient region. The magnitude of the inward pinch is increased with the density gradient larger than the linear threshold given by the electron drift wave mode theory. The contribution of the inward particle fluxes was found to exist even in the nonlinear phase. The amplitude keeps increasing in the nonlinear phase after the flattening of the pressure profile by the ballooning mode in the normal density region.

References

[1] B. Coppi and C. Spight, Phys. Rev. Lett. **41**, 551 (1978).
[2] M. Yagi, *et al*., Proc. BPSI Meeting, 2-1 (2018).
[3] M. Yagi, *et al.*, 26th IAEA FEC, TH/P3-21 (2016).
[4] C. T. Hsu, *et al.*, Phys. Fluids **29**, 1480 (1986).

Improvements of impurity transport modelling by integrated divertor code SONIC and its application to predictive simulation of future devices

Shohei YAMOTO[1)], Kazuo HOSHINO[2)], Yuki HOMMA[1)], Tomohide NAKANO[1)], Ryuichi SANO[1)] and Nobuhiko HAYASHI[1)]

[1)]QST, [2)]Keio Univ.

SONIC is one of integrated edge-plasma transport codes, which consists of the fluid plasma transport code SOLDOR, the kinetic neutral transport code NEUT2D and the kinetic impurity transport code IMPMC. One of the most unique features of SONIC is to compute the impurity transport processes kinetically. Implementing Multiple-Program Multiple-Data (MPMD) parallel computing technology enables SONIC to track independently the transport of multiple impurity species by launching IMPMC modules. Furthermore, time-dependent solver is implemented in SONIC, so that temporal impurity transport can be analyzed. With these advanced features, SONIC has been used for divertor operation scenario development for JT-60SA and the JA DEMO.

In this study, we have applied the time-dependent version of SONIC to the transient analysis of additional injection of Ne into Ar-seeded plasma in JT-60SA. In Ar-only case, the Ar impurities are stagnated in top of the SOL due to the thermal force, which are the main source of impurities into the core. It is found that only a small amount of Ne injection to the Ar seeded plasma suppresses the Ar transport along the SOL plasma towards the top of the plasma; this is mainly caused by the enhanced friction force due to the higher D^+ parallel flow in the high-field-side SOL towards the inner divertor. Figure 1 shows the Ar radiation power p_{Ar} and the parallel D^+ flow velocity $u_{//,D+}$ plotted along the field line 3.0 mm outside from the separatrix at the outer midplane at the typical snapshots. As seen from figure 1, the acceleration of $u_{//,D+}$ towards inner divertor plasma can be seen especially in the HFS near the X point, where the Ar radiation power was low. The initial Ne radiation takes place in the region where the Ar radiation power is low.

In summary, the possible mechanism of the screening of Ar by additional Ne injection is as follows:

(i) The Ne radiation takes place where Ar radiation power is low at the HFS near X-point.

(ii) The Ne radiation cooling induces initial acceleration of $u_{//,D+}$ towards inner divertor.

(iii) The ion energy is transported towards inner divertor by accelerated $u_{//,D+}$ as a convection, which mitigates the deceleration of $u_{//,D+}$ and $u_{//,D+}$ become higher.

(iv) The friction force pushes Ar ions towards inner divertor by the high $u_{//,D+}$. The highly charged Ar ions also contributes to the radiation cooling at the HFS near X-point. The Ne ions are also transported towards inner divertor and thus both Ar and Ne impurities complements the low radiation power regions of each impurity species and the $u_{//,D+}$ is further accelerated.

(v) More ion energy is also transported towards inner divertor by the convection and deceleration of $u_{//,D+}$ is further mitigated and leads to the decrease of Ar radiation and density at the top of SOL.

The time dependent analysis suggest that the additional Ne injection into Ar-seeded plasma is a possible channel to control impurity transport in the SOL.

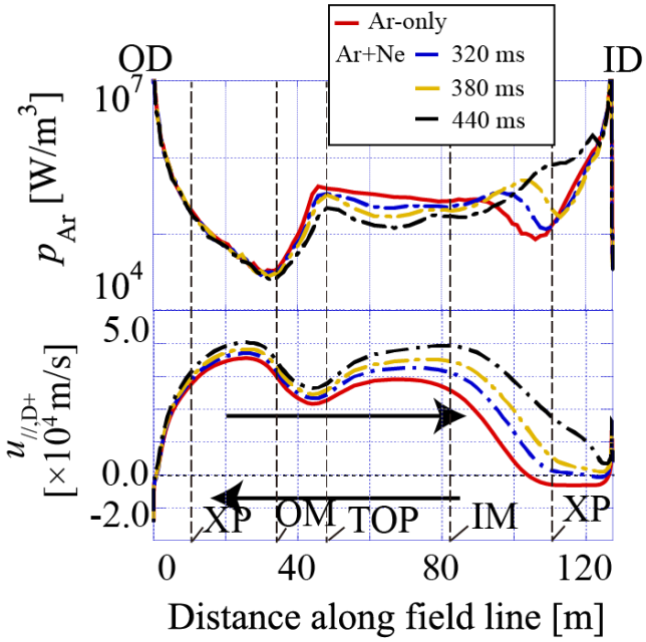

Figure 1. Ar radiation power p_{Ar} and parallel D^+ flow velocity $u_{//,D+}$ plotted along field line 3.0 mm outside from separatrix at outer midplane

Simulation of 3-D perturbation measurement in torus plasmas using a heavy ion beam probe

R. Yoshihara[1], N. Kasuya[2], T. Ido[2], M. Nunami[3], K. Fujita[3], S. Satake[3]

[1]IGSES, Kyushu University, Kasuga, Fukuoka 816-8580, Japan

[2]RIAM, Kyushu University, Kasuga, Fukuoka 816-8580, Japan

[3]NIFS, Toki, Gifu 509-5292, Japan

1. Introduction

Improving plasma confinement is important to realize fusion power generation. Plasma turbulence in torus plasmas contributes to torus transport phenomena, and its three-dimensional aspect needs to be clarified by experimental measurements. The transport phenomena are evaluated quantitatively by synthetic diagnostics, which numerically reproduce experimental measurements using simulation data [1]. It is effective to perform numerical diagnostics on multiple types of simulation data in order to elucidate various aspects of magnetically-confined plasmas. We are developing an integrated numerical diagnostics platform that can apply multiple analysis methods to multiple simulation data.

Here, we present numerical diagnostics of heavy ion beam probe (HIBP) for the Large Helical Device (LHD) and the PLATO tokamak [2]. Numerical diagnostics are performed by developing HIBP routines to three different data sets obtained by 3-D simulation code FORTEC-3D, MIPS, and R4F.

2. Heavy Ion Beam Probe

HIBP is a measurement instrument that can obtain information on the potential, density and magnetic field inside of the plasma. Injected (primary) beam of univalent (1+) heavy ions becomes to be divalent (2+) ions due to collisional ionization with plasma particles, and measurement of this (secondary) beam gives information at the ionization point [3]. Difference in kinetic energy between the primary and secondary beams corresponds to the potential at the ionization point, and density fluctuation is related to time variation of the secondary beam intensity.

3. Measurement simulation

To simulate a HIBP measurement, three-dimensional information of the magnetic field, plasma potential, density, and temperature in the measurement space is required. 3-D field data, obtained from FORTEC-3D [4], MIPS [5], and R4F [6] codes, are used for numerical analysis here.

The FORTEC-3D code is a drift kinetic code that generates distribution data on the magnetic flux coordinates (ρ, θ, ζ). The MIPS code is a 3-D MHD simulation code that generates 3-D data with spatial meshes in the toroidal coordinates (R, Z, ϕ) with equal intervals. The R4F code is a four-field reduced MHD simulation code that uses spectral expansion in the poloidal and toroidal directions and differential equations in the radial direction. Thus, each simulation code handles different physical

quantities and data formats. It is necessary to use other models or assumptions, if missing physical quantities exist. Different codes use different coordinate systems, but analysis routines to minimize information losses are required for the synthetic diagnostic simulations.

The simulator, which simulates the HIBP measurement, calculates the trajectories of the probe heavy ions, and evaluates the potential and density including path integral effects along the trajectories. The simulator can compare the physical quantities obtained from evaluation with and without turbulence in 3-D magnetic field configuration. The simulator can also include the measurement error in experiments for discussing observability of target phenomena.

4. Measurement simulation result

First, we describe simulations of the mean profile measurement, which were performed for PLATO tokamak and LHD helical plasmas. Here, we present the results of LHD plasma by using FORTEC-3D data. The data include a non-uniform electrostatic potential Φ_1 on the magnetic surface obtained from global neoclassical calculations [7]. The probe ions are monovalent gold ions Au+ injected with energy of 5.5 [MeV]. Figure 1 shows the ion trajectories, where the red circles represent the ionization points. Figure 2(a) shows difference between the observed potential and the mean potential, which corresponds to Φ_1. Figure 2(b) shows that the beam intensity is expected to be larger than the instrumental noises. The beam intensity is smaller in the low field side, because the beam path length is longer and the beam attenuation is larger in these cases.

Next, we describe the fluctuation measurement simulation. Figure 3(a) shows the time evolution of the electrostatic potential extracted from resistive drift wave turbulence data calculated by R4F. The calculation error is less than 1 [V], and the gradual change associated with the background profile change and the local fluctuation component with a period of about $100t_A$ are captured. Figure 3(b) shows the time evolution of the detected beam current intensity, when the ballooning instability calculated by MIPS causes a global pressure change. In this case, the density change at the ionization point and the time evolution of the detected beam intensity are quite different, because the density decreases largely at the central region of the plasma and the density change along the beam path is larger. This is the case when the path integral effect cannot be ignored.

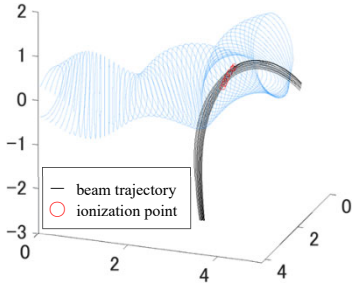

Fig. 1 Heavy ion beam trajectories in the LHD configuration.

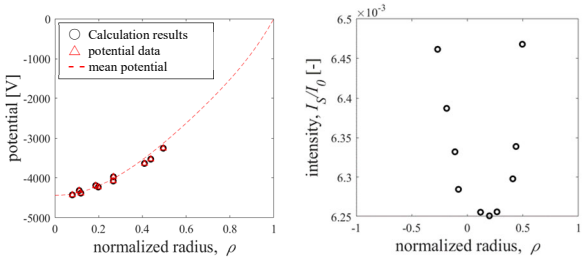

Fig. 2 Radial profiles of (a) the electrostatic potential and (b) detected beam current intensity for HIBP simulation in LHD. The positive and negative radius in (b) corresponds to positions at low and high field sides compared to the magnetic axis.

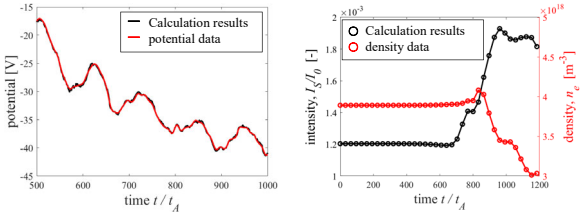

Fig. 3 Time evolutions of HIBP simulations in PLATO. (a) The electrostatic potential using R4F data at a local point ($\rho = 0.37$) and (b) the detected beam current intensity using MIPS data are shown.

References

[1] C. Holland, *et al.*, Phys. Plasmas **16** (2009) 052301.

[2] A. Fujisawa, AIP Conf. Proc. **1993** (2018) 020011.

[3] T. Ido, *et al.*, Rev. Sci. Instrum. **77** (2006) 10F523.

[4] S. Satake, *et al.*, Plasma Fusion Res. **3** (2008) S1062.

[5] Y. Todo, *et al.*, Plasma Fusion Res. **5** (2010) S2062.

[6] M. Yagi, *et al.*, Plasma Fusion Res. **2** (2007) 025.

[7] K. Fujita, *et al.*, Nucl. Fusion **61** (2021) 086025.

Analysis of transport in PANTA by Multi-field SVD

T. Kodahara[1], M. Sasaki[1], Y. Kawachi[2], Y. Jazima[1], T. Kovayashi[2], T. Yamada[3], H. Arakawa[3]
CIT, Nihon Univ.[1], NIFS[2], Kyusyu Univ[3].

1. Introduction

Performance of magnetized plasma is dominated by turbulence driven transport. Modal decomposition into a few degrees of freedom on real space is easier to understand detailed spatio-temporal dynamics. SVD enables us to analyze interactions between modes.

In this study, we apply a newly proposed method to analyze the correlation among multiple physical quantities in a data-driven manner, which is an extension of the conventional SVD method. The spatial mode structure with a common temporal evolution can be derived by the proposed method. The method is applied to a set of experimental data of the ion saturation current and the floating potential observed in a linear magnetized plasma, PANTA. Turbulence driven particle transport driven is investigated with this method.

2. Multi-field SVD

We define the spatio-temporal matrix, which consists of the ion saturation current and the radial flow. here, radial flow is evaluated from the floating potential with the assumption of E×B drift velocity. The matrix is given as

$$\Phi_{ij} = \begin{pmatrix} \mathrm{N}(\theta_1, t_1) & \mathrm{N}(\theta_1, t_2) & \cdots & \mathrm{N}(\theta_1, t_n) \\ N(\theta_2, t_1) & \mathrm{N}(\theta_2, t_2) & \cdots & \mathrm{N}(\theta_2, t_n) \\ \vdots & \vdots & \ddots & \vdots \\ \mathrm{N}(\theta_{m_1}, t_1) & \mathrm{N}(\theta_{m_1}, t_2) & \cdots & \mathrm{N}(\theta_{m_1}, t_n) \\ \mathrm{Vr}(\theta_1, t_1) & \mathrm{Vr}(\theta_1, t_2) & \cdots & \mathrm{Vr}(\theta_1, t_n) \\ \mathrm{Vr}(\theta_2, t_1) & \mathrm{Vr}(\theta_2, t_2) & \cdots & \mathrm{Vr}(\theta_2, t_n) \\ \vdots & \vdots & \ddots & \vdots \\ \mathrm{Vr}(\theta_{m_2}, t_1) & \mathrm{Vr}(\theta_{m_2}, t_2) & \cdots & \mathrm{Vr}(\theta_{m_2}, t_n) \end{pmatrix} \quad (1)$$

, where N and V_r are the ion saturation current and the radial flow, respectively. The fluctuation data is measured by the 64 channels probe array which is placed in the azimuthal direction at the fixed radial r=4cm in linear plasma device, PANTA . The azimuthal position of the observation is demoted by θ_j (j=1～32) [1]. The SVD is applied to the matrix in order to obtain the spatial mode structures of the ion saturation current and the radial flow with the common temporal evolution. The matrix is decomposed as

$$\Phi_{ij} = \sum_{k=1}^{m_1+m_2} U_{ik} \Sigma_{kk} V_{kj}^T. \quad (2)$$

Here, Σ is the singular value matrix which is the diagonal matrix, and the diagonal component $\sigma_1 \sim \sigma_{m_1+m_2}$ is sorted in descending order ($\sigma_1 \geq \sigma_2 \geq \cdots \sigma_{m_1+m_2}$)[2,3]. The matrix U corresponds to the spatial structure. The matrix ΣV^T has the temporal evolution of turbulence common to the ion saturation current and the radial flow. the above method is based on orthogonal bases in a data-driven manner.

3. Transport analysis by Multi-field SVD

Based on the Eq. (1), fluctuation data of the ion saturation current and the flow are combined in spatial direction, and the singular value decomposition (SVD) is applied to the combined observation matrix. This is the Multi-field SVD, where the common characteristics can be deduced between the different physical quantities. The spatial structures U_{ik} with common temporal evolution $\Sigma_{kk}V^{T}_{kj}$ of fluctuation of the density and the radial flow are evaluated, are shown Fig. 1. The phase of both spatial structures can be systematically evaluated. This phase difference is appeared in disposition of typical resistive drift wave [4].

Mode α of the density and mode β of the radial flow obtained from results of Multi-field SVD is respectively defined as N_{α} and $V_{r\beta}$, and transport is evaluated by the following

$$< \tilde{\Gamma}_r >= \sum_{\alpha,\beta} < \overline{N_{\alpha} V r_{\beta}} > \quad (3)$$

In addition, the results of conventional SVD is applied to Eq. (3) to evaluate transport. In the Multi-field SVD and the conventional SVD, the transport which the combination of the such mode drives is shown in the Fig. 2. Transport using results of Multi-field SVD is evaluated at only combinations of mode satisfying $\alpha = \beta$. Transport using result of conventional SVD is complicated because transport is caused by combinations of various mode. It can be said important to simultaneously analyze fluctuation of the density and the radial flow because of stemming from the mode orthogonality of the SVD. Multi-field SVD also enable to greatly reduce the number of combinations of mode.

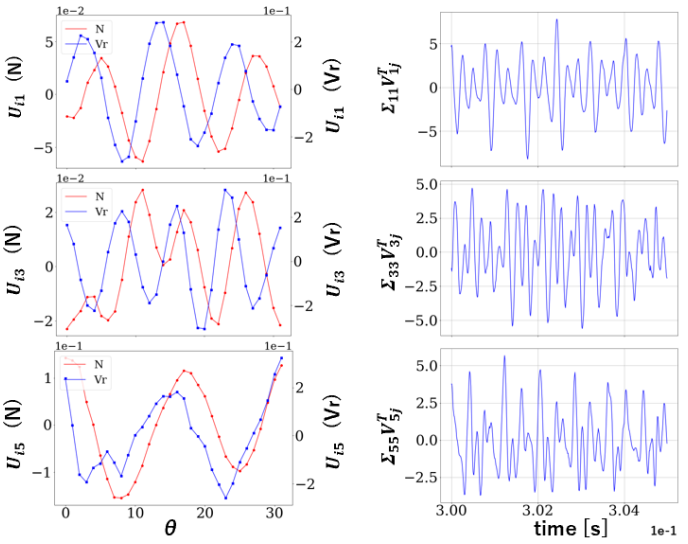

Fig. 1 (Left panel) The spatial structure of mode1,3,5. (Right panel) The common temporal evolution of N and Vr of mode 1,3,5.

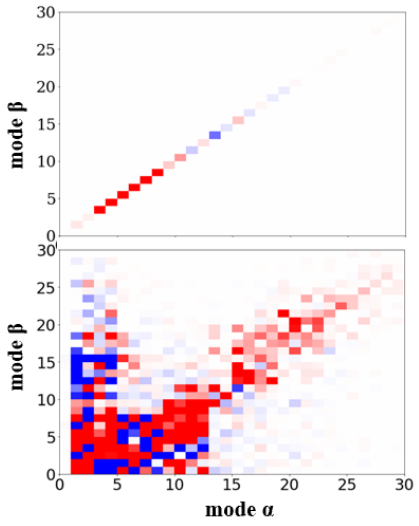

Fig. 2 The transport which the combination of the such mode drives, using results obtained from the Multi-field SVD (left panel) and the conventional SVD (right panel)

References

[1] T. Yamada, et al, Nature Physics, 4.9, 721-725, (2008)

[2] M. Sasaki, et al, Plasma Physics and Controlled Fusion, 63.2, 025004 (2020)

[3] Y. Asahi, et al, Physics of Plasma, 28.1, 012304, (2021)

[4] W. Horton, et al, Reviews of Modern physics, 26.4, 042306, (2019)